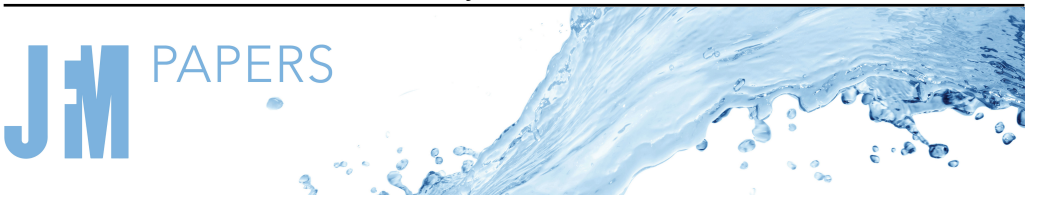
J. Fluid Mech. (2026), *vol.* 1046, A14, doi:10.1017/jfm.2026.12185



Screech in rocket nozzles undergoing free shock separation

Chi Co Tran[1], **Petrônio Nogueira**[1], **Joel Weightman**[1] and **Daniel Edgington-Mitchell**[1]

[1]Department of Mechanical and Aerospace Engineering, Shock Lab, Monash University, Melbourne, VIC 3800, Australia

Corresponding author: Chi Co Tran, tranchico178@gmail.com

(Received 13 April 2026 UTC; revised 31 July 2026 UTC; accepted 7 September 2026 UTC)

Flow separation in rocket nozzles generates intense side loads that can lead to structural damage affecting space flight safety. Recent studies have hypothesised that a screech-like resonance loop may be responsible for such oscillations in the free shock separation (FSS) regime. In this work, we aim to confirm if screech is indeed present in this flow. Five thrust-optimised parabolic nozzles with different length and area ratios were examined at a nozzle pressure ratio range where FSS was expected to occur. Spectral proper orthogonal decomposition (SPOD) revealed resonance for both $m = 0$ and $m = 1$ azimuthal modes. Further decomposition of the SPOD modes allowed for the identification of downstream- and upstream-travelling waves, whose characteristics match the description of the Kelvin–Helmholtz (KH) instability wave and the guided jet mode (GJM), respectively. Linear stability analysis performed on Reynolds-averaged Navier–Stokes mean-flow fields confirms the existence of these two waves for the conditions studied and provides insight into their dispersion relation. A well-validated screech predictive model was employed and accurately predicted the resonant frequencies. The accurate predictions, combined with the observation of the KH and GJM waves, confirm that screech is active in this flow.

Key words: aeroacoustics, shock waves, shear-flow instability

1. Introduction

Flow separation has been known to generate deleterious side loads on the nozzle wall during the start-up phase of rocket engines. In these operating conditions, the flow faces

© The Author(s), 2026. Published by Cambridge University Press. This is an Open Access article, distributed under the terms of the Creative Commons Attribution licence (https://creativecommons.org/licenses/by/4.0/), which permits unrestricted re-use, distribution and reproduction, provided the original article is properly cited.

https://doi.org/10.1017/jfm.2026.12185 Published online by Cambridge University Press

an adverse pressure gradient due to the mismatch between the ambient and nozzle wall pressure, causing it to separate from the wall, resulting in a complex flow structure. The unsteady and oscillatory nature of this flow leads to the generation of side loads, which can be harmful to the rocket structure (Nave & Coffey 1973). While recent studies have improved the understanding of this phenomenon, the mechanism that underpins the unsteady oscillation still requires further investigation to be fully characterised.

There are two distinct separation patterns in rocket nozzles, as identified in the early work of Nave & Coffey (1973). The first one is free shock separation (FSS), which typically occurs in a wide range of nozzle contours at low nozzle pressure ratios (NPRs), when the flow is highly overexpanded. In this pattern, the expanding supersonic flow separates from the nozzle wall due to an adverse pressure gradient, forming a separation shock and a supersonic annulus. Diverted by a reflected shock, which originates from the triple point, this annulus then wraps around a subsonic core located aft of the Mach disk. The second pattern is restricted shock separation, which occurs at higher NPRs. It is less common, as it only manifests in specific nozzle types, such as thrust-optimised parabolic (TOP) and thrust-optimised contour nozzles. In these nozzles, due to the steep divergence angle of the nozzle wall, an internal shock is formed, which interacts with the Mach disk, inducing a reflected shock. The resulting reflected shock then provides the separated flow with extra radial momentum, diverting it towards the nozzle wall (Frey & Hagemann 1999). As a result, the flow structure comprises a large Mach disk and a supersonic annulus that reattaches to the nozzle wall after the separation point. The region bounded by the separation and reattachment points of this annulus is known as the separation bubble. In the work of Frey & Hagemann (1999), this pattern was termed the 'cap-shock pattern'.

It has been known that side loads on nozzle walls are induced by the unsteady asymmetric oscillation of separation shocks (Schmucker 1984; Dumnov 1996). However, the precise mechanism through which this oscillation is triggered remains an open question. One attempt to address this involved investigating the shock wave–boundary-layer interaction as a potential cause for this phenomenon. These studies hypothesised that the unsteadiness that drives the oscillations is caused by the interaction between the boundary layer of the expanding flow and the separation shock (Baars *et al.* 2012). The characteristic of this interaction, also corroborated in Baars & Tinney (2013), is manifested as two distinct broadband humps in the wall dynamic pressure spectra, where the low-frequency hump is associated with the oscillation of the shock structure and the high-frequency hump is linked to the instabilities within the supersonic shear layer.

Extending the work of Baars & Tinney (2013) to the FSS regime, Jaunet *et al.* (2017) computed the power spectral density (PSD) of the wall pressure fluctuation on a truncated ideal contour (TIC) nozzle as a function of NPRs. The work confirmed the presence of the aforementioned humps, and a discrete peak in the intermediate frequency range $St = 0.2$ was detected. This peak corresponds to a highly coherent structure in both time and azimuth that persists downstream. Notably, azimuthal decomposition revealed that this structure manifests as an $|m| = 1$ mode, suggesting its involvement in the side-load generation mechanism. Furthermore, the close alignment between these peak frequencies and the semi-empirical screech prediction model proposed by Tam *et al.* (1986) led the authors to speculate that a screech-like resonance loop could be present in this flow and that it could contribute to the side-load generation process. Since no distinct tonal sound was detected, which is the signature of jet screech, the authors hypothesised a pseudo-screech mechanism where the energy transfer processes occur in the subsonic core. In this case, the supersonic annulus acts as a mask, preventing acoustic waves from escaping to the ambient field.

https://doi.org/10.1017/jfm.2026.12185 Published online by Cambridge University Press

The work of Jaunet *et al.* (2017) led to several subsequent studies aimed at exploring these findings. Martelli *et al.* (2020), via a delay-detached-eddy simulation of a TIC nozzle in the FSS regime, reaffirmed the presence of the intermediate peak and proposed a self-sustaining mechanism for this resonance. They hypothesised that starting from the Mach disk and the triple point, vortices are ejected and travel downstream until they interact with the second normal shock, emitting acoustic waves that propagate upstream, closing the loop. Subsequently, Bakulu *et al.* (2021) built upon these findings by investigating the flow structure associated with the peak frequency. Using synchronised and time-resolved data of external jet velocity and wall pressure, the authors observed a strong coherence between the wall pressure signal and jet velocity fluctuation at this frequency. And via spectral proper orthogonal decomposition (SPOD), upstream- and downstream-travelling waves were detected, confirming the essential ingredients for a resonance loop. Additionally, the authors found that even though these waves only contribute 20 % of the side-load generation, they can induce the oscillation of the shock structure, which generates the remaining side loads.

Most recently, Jaunet & Lehnasch (2025) performed linear stability analysis (LSA) of an FSS analytical base flow. Via the analysis, the authors discovered that the flow can support two unstable downstream-travelling Kelvin–Helmholtz (KH) waves associated with the outer and inner shear layers of the supersonic annulus. The former is more unstable, and the latter is more sensitive to the variation of the mean-flow profile. They speculated that the inner KH wave might be important for sustaining the resonance, as this wave exhibits radial support in the jet outer region, which permits energy transfer with the upstream-travelling waves. The upstream-propagating guided jet mode (GJM) (Nogueira *et al.* 2024), which was proven to close the screech loop as shown in recent studies (Edgington-Mitchell *et al.* 2018; Gojon *et al.* 2018), was also found to be supported by the flow for a wide range of jet Mach numbers. However, at the operating condition and frequency at which the resonance was observed ($M_j = 2.09$, $St = 0.2$), the GJM was not supported by the flow. For this specific condition, the GJM was found to be supported at a lower-frequency range. As a consequence, this work could not link the experimentally observed resonance loop with the characteristics of a screech loop. The authors argued that this could be due to the base-flow approximation not being sufficiently accurate, or to the simplifications and assumptions of the model, which led to the inability to capture these waves at the resonant frequency (Jaunet & Lehnasch 2025).

Screech (Raman 1999; Edgington-Mitchell 2019) is a distinct tonal sound produced by a resonance loop formed in shock-containing jets. This loop starts with the downstream convection of the unstable KH wavepacket, which harnesses energy from the mean flow as it grows. This wave then interacts with the shock-cell structure downstream, resulting in an energy transfer to the upstream-travelling disturbances. These disturbances then propagate to a sensitive region of the flow and create perturbations in the shear layer, closing the loop. Several models have been developed aiming to predict the screech frequency (Powell 1953; Panda 1999). Notably, the weakest-link model proposed by Tam *et al.* (1986) posits that the interaction between the KH wavepacket and the quasi-periodic shock structure can transfer energy to certain upstream-propagating wavenumbers via the triadic interaction mechanism, which can be mathematically expressed as

$$k_{up} = k_{KH} \pm k_{sh}. \tag{1.1}$$

Here, k_{up}, k_{KH} and k_{sh} are the upstream-propagating wavenumber, the KH wavepacket wavenumber and the shock-cell wavenumber, respectively. It should be noted that until recently, it was assumed that the free-stream acoustic wave, not the GJM, played a role as the upstream-propagating disturbances, which is also the case for the weakest-link model.

https://doi.org/10.1017/jfm.2026.12185 Published online by Cambridge University Press

Despite the difference in the upstream-travelling wave, the key concept of energy transfer via the triadic interaction embedded in the model is well validated (Edgington-Mitchell *et al.* 2021; Nogueira *et al.* 2022*b*). As demonstrated in the work of Nogueira *et al.* (2022*b*), screech arises from an absolute instability mechanism where the periodicity in the mean flow, induced by the shock-cell structure, enables the triadic interaction to occur. To apply the recent changes in the understanding of screech, Nogueira *et al.* (2022*a*) suggested two modifications to the weakest-link model. The first modification introduces an additional requirement for screech to occur, that the triadic interaction between the KH wave and shock structure must transfer the energy to the wavenumbers that the GJM is supported by the flow:

$$k_{GJM} = k_{KH} \pm k_{sh}. \tag{1.2}$$

In this formulation, k_{GJM} is the GJM wavenumber. The second modification was to consider the streamwise variation of the shock structure in making a prediction rather than using a single shock-cell wavenumber k_{sh}. Incorporating these modifications into the original weakest-link model results in a robust model that effectively explains jet screech. In this paper, this modified model will be referred to as the screech triadic interaction model (STIM).

In light of the recent evidence indicating that a potential screech-like resonance loop might play a role in generating side loads in the FSS regime, extending from previous work (Tran *et al.* 2024, 2026), the present study aims to confirm the mechanism for this resonance loop. The content of this paper is organised as follows. The experimental and numerical approaches are described in § 2. The results are presented in §§ 3 and 4. And finally, the conclusions are drawn in § 5.

2. Methodology

2.1. *Experimental approach*

In this work, five TOP nozzles with a throat diameter $D_t = 10$ mm were investigated, whose specifications are shown in table 1. Here, AR is the area ratio of each nozzle, which is defined as the ratio between the exit and throat areas (A_e/A_t). Diameter D_e is the exit diameter, L_n is the axial distance between the throat and the exit of each nozzle and ψ is the mean nozzle divergence angle ($\psi = \arctan((D_e - D_t)/(2L_n))$). For brevity, from this point onward, the term 'divergence angle' will be used and should be interpreted as the mean divergence angle. The nozzles were named such that the digit after letter 'A' indicates the AR of the nozzle and the digits after letter 'L' indicate L_n in terms of the percentage compared with that of an ideal nozzle designed by the method of characteristic (Rao 1958). For instance, nozzle TA2L6 has an AR of 2 and an L_n of 60 % compared with L_n of an ideal nozzle with the same AR. The nozzles were operated under cold-flow conditions with pressure ratios of NPR $= p_0/p_\infty = [2:6]$, where p_0 is the stagnation pressure of the chamber and p_∞ is the ambient pressure. In this NPR range, the flow for all nozzles manifested an FSS pattern, which was based on observations from numerical simulations (discussed in § 2.2). These operating conditions yield a Reynolds number range of $Re = D_j U_j/\nu_\infty = [2.25 \times 10^5 : 4.05 \times 10^5]$. Here, D_j is the ideally expanded nozzle diameter, U_j is the ideally expanded jet exit velocity and ν_∞ is the ambient air kinematic viscosity. It can be seen that AR and L_n of these nozzles are relatively low compared with a full-scale rocket nozzle. This was an intentional design so that the separation points are close to the nozzle exit and the majority of the flow structure is located outside of the nozzle for visualisation. A cylindrical coordinate system is used in this study, as shown in figure 1 along with the cross-section of nozzle TA6L8. Here, the

https://doi.org/10.1017/jfm.2026.12185 Published online by Cambridge University Press

Nozzle	AR	D_e (mm)	L_n (mm)	ψ (deg.)
TA2L6	2	14.1	4.6	24.1
TA2L8	2	14.1	6.2	18.5
TA2L15	2	14.1	11.6	10.1
TA4L8	4	20.0	14.9	18.5
TA6L8	6	24.5	21.6	18.5

Table 1. List of nozzle dimensions.

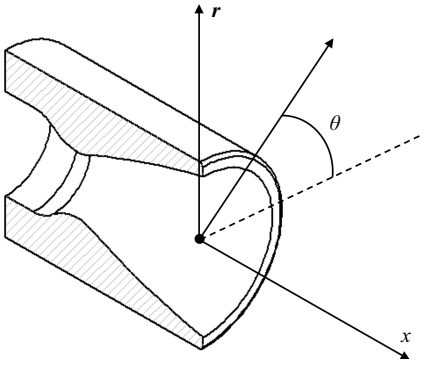


Figure 1. Cross-section of the TA6L8 nozzle along with the coordinate system used in this study.

origin is located at the centre of the nozzle exit, x is the axial direction measuring from the nozzle exit, r is the radial direction measuring from the centreline of the jet and θ is the azimuthal direction. In this work, both x and r coordinates were non-dimensionalised by D_j. As the focus is on proving the existence of a screech-like resonance loop by performing the analysis on an axisymmetric mean flow, and the directionality of the side loads or the acoustic field of the resonance loop is not considered, the azimuthal direction (θ) is omitted in the analysis.

Flow visualisation was performed using a Z-type Toepler schlieren facility. Images with light intensities proportional to path-integrated density gradients $\partial\rho/\partial x$ were captured using a Photron Fastcam SA-Z 2100k camera. The image acquisition rate was set to 240 kfps leading to a Nyquist frequency of 120 kHz. The spatial resolution of the images is 384×131 pixels with a field of view spanning $\approx 12\ D_t$ downstream and $\approx 2\ D_t$ in the radial direction, from the centreline of the jet. The flow field was illuminated using a pulsed LED with a pulse width of 500 ns (Willert *et al.* 2012). At each operating condition for each nozzle, 100 000 samples were recorded. Here, SPOD (Lumley 1970; Towne *et al.* 2018) was performed on all schlieren images, and the spatial mode shapes ϕ of the coherent structures at the resonant frequencies were extracted. The Welch method (Welch 1967) was applied to obtain the spectral contents of the flow with a window of 2048 sampling points and 50 % overlap between adjacent segments. It should be noted that SPOD was performed on schlieren light intensities, which do not directly yield the energy content of the coherent structures. However, the light intensity in the schlieren image is proportional to the strength of the gradient, and consequently the SPOD algorithm is still able to

https://doi.org/10.1017/jfm.2026.12185 Published online by Cambridge University Press

Mesh	Number of elements
Coarse	176 433
Medium	305 596
Fine	628 931

Table 2. Specifications of the meshes used in the mesh convergence study.

identify the highest-amplitude structures, despite the eigenvalues themselves not being meaningful in a quantitative sense.

2.2. *Generation of numerical mean flow*

Reynolds-averaged Navier–Stokes (RANS) equations were employed to obtain the essential mean-flow-field properties that will be used for LSA (described in § 2.3). For each nozzle, the RANS calculations were conducted for NPRs = [3, 3.5, 4, 4.5, 5] as these cases contain all the significant flow physics discussed in §§ 3 and 4. Simulations were performed assuming axisymmetric flow for all cases to reduce computational cost, and improve convergence of the resulting mean flows. The domain covered an area spanning $\approx 35\ D_t$ axially downstream (from the nozzle exit) and $\approx 10\ D_t$ radially (from the centreline). The computational field was initialised using room conditions with an atmospheric pressure of $p_a = 101\,325$ Pa and ambient temperature of $T_a = 300$ K. At the inlet, a total pressure p_0 boundary condition was applied, followed by a stagnation temperature $T_0 = 300$ K, which is consistent with the cold-flow operating conditions of these nozzles in the experiments. The outlet conditions were treated as zero gradient, as the simulation domain is much larger than the jet. No-slip conditions were applied at the nozzle wall. In the calculations, air was modelled as an ideal gas with a constant specific heat $c_p = 1004.5\ \text{J (kg K)}^{-1}$ and a specific heat ratio of $\gamma = 1.4$.

To balance between computational efficiency and accuracy, the meshes were refined for the regions within the nozzles and downstream jet where the significant features of the flow are concentrated. Sixty prism layers with the first layer thickness of $\Delta h/D_t = 2 \times 10^{-5}$ were applied at the nozzle wall, resulting in $y^+ \leq 1$ for all cases, which ensures the boundary layer is sufficiently resolved. Grid-independent solutions were confirmed via a mesh convergence study. Details of the mesh specifications and RANS results of this study are shown in table 2 and figure 2. In this work, the fine mesh setting was used for all simulations. The RANS equations were spatially discretised using second-order upwind and second-order central-differencing schemes for the advection and diffusion terms, respectively, while the implicit first-order Euler scheme was used for temporal marching. The governing equations were then solved using a density-based solver prebuilt in OpenFOAM$^{\text{TM}}$ (Greenshields 2023).

A $k-\omega$ SST model was used to account for the turbulence effect, which was selected due to its robustness in calculations of flow separation in rocket nozzles as demonstrated in the work of Stark & Hagemann (2007). The governing equations for this model and their associated parameters can be found in Menter *et al.* (2003). The model parameters were carefully tuned such that the shock-cell structure was accurately captured for all cases. The tuning processes were conducted with Bayesian optimisation (Shahriari *et al.* 2016) employed using Deker software (Linossier 2025) to minimise the cost function:

$$C = \sqrt{0.7\left(k_{sh1_R} - k_{sh1_e}\right)^2 + 0.3\left(k_{sh2_R} - k_{sh2_e}\right)^2}. \tag{2.1}$$

https://doi.org/10.1017/jfm.2026.12185 Published online by Cambridge University Press

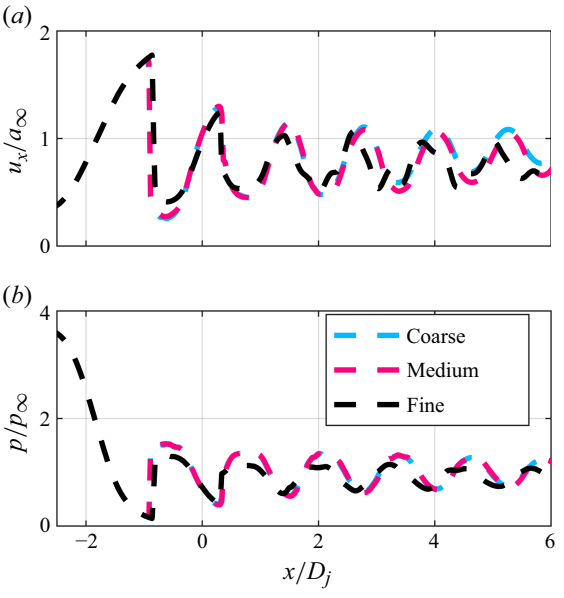


Figure 2. The RANS results for the TA6L8 nozzle at NPR = 4 for different meshes with (*a*) centreline velocity normalised by the ambient speed of sound and (*b*) centreline pressure normalised by the ambient pressure.

Here, the subscripts R and e denote the RANS and experimental values, respectively. As the goal is to match the shock-cell structure, the shock wavenumbers (k_{sh}) were selected as the inputs for the cost function (C). These values can be obtained by performing axial Fourier transforms on the streamwise pressure variations along the jet centreline (i.e. the local static-pressure deviation from the streamwise-averaged centreline pressure) for RANS data and directly on the pixel intensities of the mean schlieren images for experimental data. The subscripts 1 and 2 represent the primary and secondary peaks in the shock-cell wavenumber spectrum, respectively. The weights used in this cost function are subjectively chosen to have a bias for the k_{sh1} residual but not completely neglecting the accuracy of k_{sh2}. More weight was set for the k_{sh1} residual due to the greater significance of accurately capturing the first few shock cells, since the important flow physics are located in this region (discussed in § 3.1).The tuned parameters for each simulation case along with the associated error can be found in Appendix C. Figure 3 demonstrates the comparison between a fine-tuned RANS simulations for nozzles TA2L15 and TA2L8 at NPR = 4 and the time-averaged schlieren images. For both cases, it can be seen that there is good agreement between the RANS simulations and experiments within this upstream region. Deviations from the experimental results can be observed further downstream, but they are expected to have a minor effect in this study. These two nozzles operating at NPR = 4 possess distinct flow structures, as will be shown in § 4. Hence, the fact that RANS simulations demonstrate close agreement with schlieren mean flow for both cases highlights the robustness and accuracy of the RANS simulations and tuning approach.

2.3. *Linear modelling strategy*

With the establishment of the mean-flow fields through RANS simulations, the waves supported by the flow can be investigated. In this work, locally parallel spatial LSA was performed for such purposes, following the assumptions stated in Michalke (1965),

https://doi.org/10.1017/jfm.2026.12185 Published online by Cambridge University Press

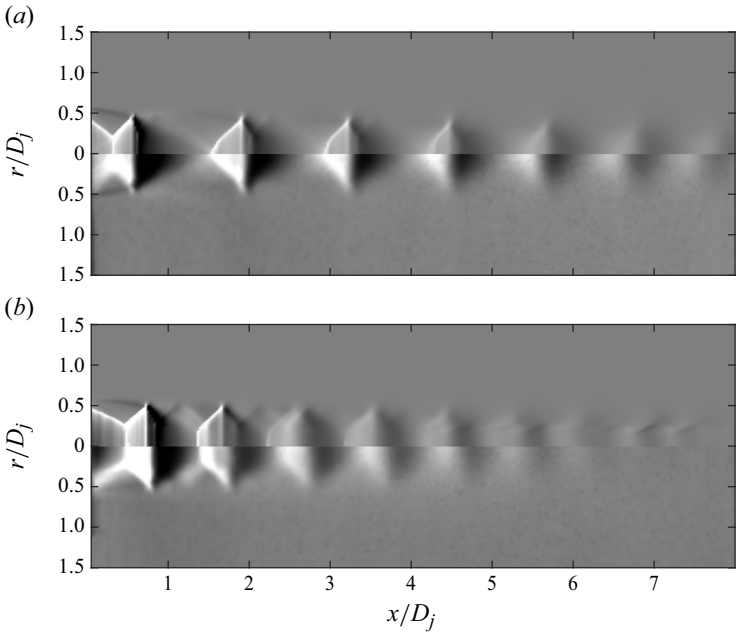


Figure 3. Shock structure comparison between RANS simulation (top half of each panel) and mean schlieren image (bottom half of each panel) at NPR = 4 for (*a*) nozzle TA2L15 and (*b*) nozzle TA2L8. The RANS streamwise density gradient was reconstructed into a three-dimensional field with axisymmetric assumption and path-integrated to facilitate the comparison.

following an approach similar to that of Ivelja *et al.* (2024). The theoretical framework for this technique is based on introducing infinitesimal disturbances into the mean flow and studying their spatial evolution. Key characteristics of the supported waves, such as the dispersion relations and growth rates, can be extracted from the analysis.

Starting with the inviscid, compressible Navier–Stokes equations in cylindrical coordinates, Reynolds decomposition was applied to the fluid variables, splitting them into the mean and fluctuating components:

$$\boldsymbol{q}(x, r, \theta, t) = \bar{\boldsymbol{q}}(r) + \boldsymbol{q'}(x, r, \theta, t). \tag{2.2}$$

Vector $\boldsymbol{q} = [v, u_x, u_r, u_\theta, p]$ represents the specific volume, axial, radial, azimuthal velocities and pressure, respectively; $\bar{\boldsymbol{q}}$ is the mean-flow vector; and $\boldsymbol{q'}$ is the disturbance vector. All variables were non-dimensionalised by the ambient speed of sound (c_∞), ambient air density (ρ_∞) and D_j. In the locally parallel framework, the mean-flow variables are only functions of the radial position (r) (Michalke 1965; Towne *et al.* 2017). The normal mode ansatz was then employed to further decompose the disturbance vector:

$$\boldsymbol{q'}(x, r, \theta, t) = \hat{\boldsymbol{q}}(r)\mathrm{e}^{\mathrm{i}(\alpha x + m\theta - \omega t)}. \tag{2.3}$$

In this ansatz, $[\alpha, m, \omega]$ correspond to the streamwise wavenumber, azimuthal wavenumber and angular frequency in that order. For spatial LSA, m and ω are real and prescribed constants while α is a complex value ($\alpha = \alpha_r + \mathrm{i}\alpha_i$) with the real component characterising the spatial wavenumber and the imaginary component characterising the spatial growth rate of the wave. The vector $\hat{\boldsymbol{q}}$ provides the spatial mode shape of the flow disturbances in the radial direction.

https://doi.org/10.1017/jfm.2026.12185 Published online by Cambridge University Press

Inserting (2.2) and (2.3) into the governing equations and neglecting the nonlinear terms results in the eigenvalue problem:

$$\boldsymbol{L}\hat{\boldsymbol{q}} = \alpha \boldsymbol{R}\hat{\boldsymbol{q}}. \tag{2.4}$$

Here, $\boldsymbol{L}$ and $\boldsymbol{R}$ are matrices representing the linearised inviscid compressible Navier–Stokes equations, which can be constructed using mean-flow properties $[\bar{v}, \bar{u_x}, \bar{p}]$ obtained from RANS simulations at desired axial locations (details of the operators are shown in Appendix D). As the flow is assumed to be locally parallel, mean-flow radial and azimuthal velocities $[\bar{u_r}, \bar{u_\theta}]$ were omitted. It should be noted that even though the flow still has a non-negligible mean radial velocity, this assumption is justifiable since the axial velocity component is much greater than the radial velocity. Moreover, as shown in Nogueira & Edgington-Mitchell (2021), locally parallel LSA still provides good agreement with experimental results even in the presence of significant mean-flow radial velocity. Chebyshev polynomials coupled with radial mapping were employed to discretise the domain in the radial direction to ensure the high grid-point density at the jet shear layers and faster convergence rates (Trefethen 2000). The calculations were performed using 250 Chebyshev points, which is sufficient for reaching mesh-independent results. In this work, $m = 0$ and $m = 1$ azimuthal modes will be considered for the computations; only screech tones associated with these azimuthal modes have been reported in the literature. Here, $\hat{\boldsymbol{q}}$ and α can be solved numerically using MATLAB's eig function. For each eigenvalue α, a corresponding eigenvector is obtained and stored in matrix $\hat{\boldsymbol{q}}$.

Finally, boundary conditions are supplied to make this eigenvalue problem well-posed. At the jet centreline, different conditions need to be applied depending on the azimuthal mode (Lesshafft & Huerre 2007). For the $m = 0$ mode, flow perturbations should follow

$$\hat{u}_r(0) = \hat{u}_\theta(0) = 0, \tag{2.5}$$

$$\left(\frac{\partial \hat{u}_x}{\partial r}\right)_{r=0} = \left(\frac{\partial \hat{p}}{\partial r}\right)_{r=0} = \left(\frac{\partial \hat{v}}{\partial r}\right)_{r=0} = 0. \tag{2.6}$$

And, for the first helical mode ($m = 1$),

$$\hat{v}(0) = \hat{u}_x(0) = \hat{p}(0) = 0, \tag{2.7}$$

$$\left(\frac{\partial \hat{u}_r}{\partial r}\right)_{r=0} = 0, \tag{2.8}$$

$$\hat{u}_r(0) \pm \mathrm{i}\hat{u}_\theta(0) = 0. \tag{2.9}$$

At the far field, where disturbances are expected to decay, Dirichlet conditions were applied for both azimuthal modes at a point $r_{max} = r/D_t = 10$ very far from the jet:

$$\hat{v}(r_{max}) = \hat{u}_x(r_{max}) = \hat{u}_r(r_{max}) = \hat{u}_\theta(r_{max}) = \hat{p}(r_{max}) = 0. \tag{2.10}$$

The radial location of the far-field boundary (r_{max}) was selected such that the results are insensitive to this choice.

However, the far-field conditions of (2.10) are not the appropriate boundary conditions for wall-bounded flows. Considering there are significant flow structures present at the wall for some nozzles at low NPRs, another set of boundary conditions was implemented to force the gradient of both pressure and specific volume to be zero at the wall, or

https://doi.org/10.1017/jfm.2026.12185 Published online by Cambridge University Press

$$\left(\frac{\partial \hat{v}}{\partial r}\right)_{r=r_{wall}} = \left(\frac{\partial \hat{p}}{\partial r}\right)_{r=r_{wall}} = 0. \tag{2.11}$$

For the velocity disturbances, no-slip conditions and impermeable wall were applied, namely

$$\hat{u}_x(r_{wall}) = \hat{u}_r(r_{wall}) = \hat{u}_\theta(r_{wall}) = 0. \tag{2.12}$$

Since the flow field considered in this study comprises the shock-cell structure, flow separation and recirculation regions, the locally parallel assumptions will certainly be violated. However, recent studies suggest that LSA can still provide accurate results even for shock-containing jets (Edgington-Mitchell *et al.* 2021; Nogueira & Edgington-Mitchell 2021; Nogueira *et al.* 2022*a*; Ivelja *et al.* 2024; Nogueira *et al.* 2025). More explicitly, in the work of Jaunet & Lehnasch (2025), using LSA, the authors have successfully characterised the waves associated with resonance in the FSS flow pattern. Thus, despite limitations, LSA is still a viable tool for examining the resonance behaviour of this flow structure.

2.4. *Resonance model*

Once LSA is performed and the characteristics of the supported waves are obtained, STIM, as proposed in Nogueira *et al.* (2022*a*), will be used to predict the screech frequency. It is important to note that the primary purpose for implementing the model is not to illustrate its predictive capability (which has been done in a series of previous works (Edgington-Mitchell *et al.* 2021, 2022; Nogueira & Edgington-Mitchell 2021; Nogueira *et al.* 2022*a*, 2025; Ivelja *et al.* 2024)), but rather to provide supporting evidence that the resonance loop observed in rocket nozzles undergoing FSS is indeed screech. Since the theoretical framework of the triadic interaction as a mechanism for the energy exchange in a screech loop has been validated, successful predictions of the experimental resonant frequencies using STIM will strongly suggest that the resonance loop is screech.

There are three inputs required for this model: the wavenumber of the KH instability ($k_{KH}(\omega)$), the wavenumber of the guided jet wave ($k_{GJM}(\omega)$) and the axial wavenumber corresponding to the shock structure (k_{sh}). The frequency that has the associated wavenumbers satisfying (1.2) is the predicted frequency of this model. The wavenumbers of the KH and GJM waves are the real components of the corresponding eigenvalues α, which can be computed directly from LSA. For k_{sh}, it has previously been demonstrated (Edgington-Mitchell *et al.* 2021; Nogueira *et al.* 2022*a*, 2025) that the triadic interaction between the shocks and the KH wavepacket can occur over different streamwise regions. Each of these regions will have its own quasi-periodicity associated with a local shock-cell wavenumber k_{sh}. In Nogueira *et al.* (2022*a*), it was demonstrated that the first suboptimal peak (k_{sh2}) often works well for resonance predictions; however, this peak is not always easy to identify if the primary peak is sufficiently broad. Edgington-Mitchell *et al.* (2022) demonstrated that the standing wave associated with screech (see also Panda 1999) will always match its wavenumber to the local k_{sh} for the region where the triadic interaction occurs. Thus, in this work, to avoid the ambiguity of selecting the appropriate peak from the shock-cell wavenumber spectrum, we will simply set the local k_{sh} equal to k_{sw}.

3. Evidence of a screech loop in FSS

3.1. *Experimental evidence*

The discussion begins with nozzle TA6L8 at NPR = 4, since this case manifests resonance in both $m = 0$ and $m = 1$ azimuthal modes (as will be proved). Figure 4 shows the

https://doi.org/10.1017/jfm.2026.12185 Published online by Cambridge University Press

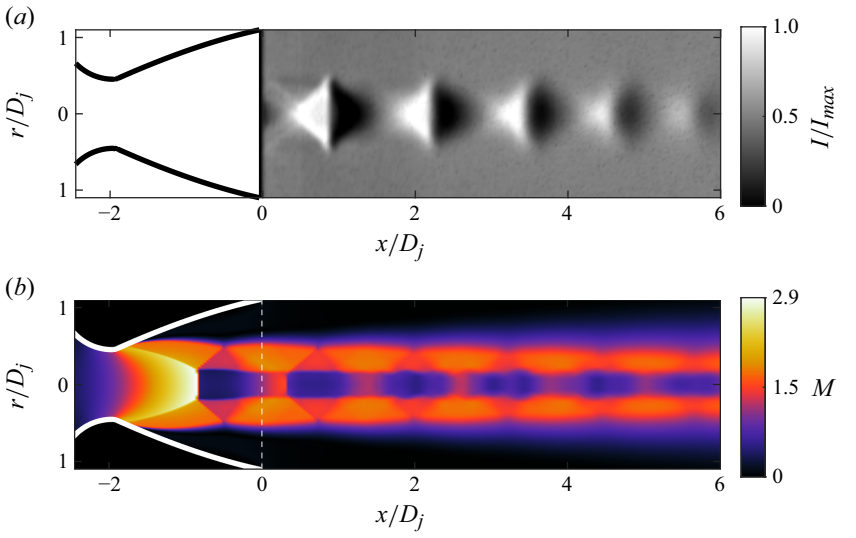


Figure 4. (*a*) Time-averaged schlieren image of nozzle TA6L8 at NPR = 4. Data were normalised by the maximum pixel intensity and rescaled. (*b*) Associated RANS Mach number field.

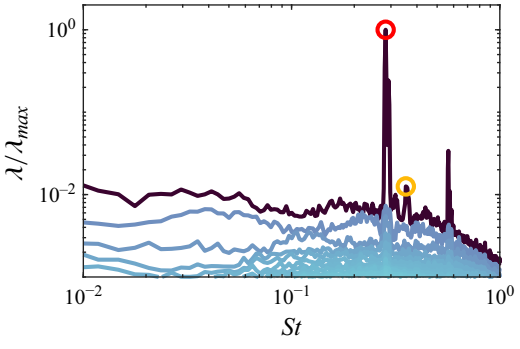


Figure 5. The SPOD spectra of nozzle TA6L8 at NPR = 4. Values were normalised by the maximum value of the first SPOD mode. Red circle: primary peak at $St = 0.283$. Yellow circle: secondary peak at $St = 0.354$. Mode order is indicated by the shade of blue, with darker blue representing lower-order (more energetic) modes.

time-averaged schlieren image for this case along with the RANS Mach number field. It can be seen that the flow exhibits the FSS pattern with the typical features visible in the RANS simulation, i.e. the separation shock, Mach disk and the supersonic annulus. As depicted in the schlieren image, the flow possesses a periodic shock structure in the axial direction, which is a key ingredient for screech to occur (Nogueira *et al.* 2022*b*).

Spectral proper orthogonal decomposition was performed on the schlieren images, and the associated spectrum for this case is presented in figure 5. Here, St is the Strouhal number, defined as $St = f D_j / U_j$, where f is the frequency (Hz). It can be seen that the first SPOD mode (dark blue line) dominates the flow dynamics for a wide range of frequencies. In this mode, there are two distinct energetic peaks manifesting in the spectra. The primary peak is at $St = 0.283$ (red circle), with its harmonic at $St = 0.566$, and a secondary peak is at $St = 0.354$ (yellow circle). At $St = 0.293$, there is another peak exhibiting the same mode shape as the primary peak. However, time–frequency analysis

https://doi.org/10.1017/jfm.2026.12185 Published online by Cambridge University Press

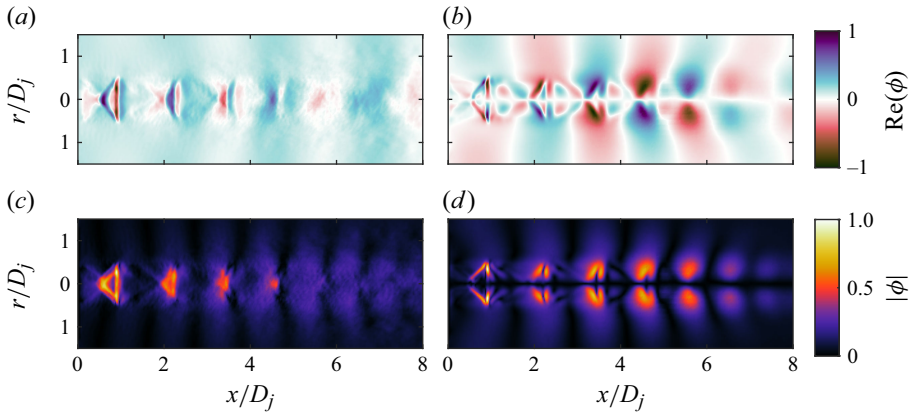


Figure 6. The SPOD mode shapes of nozzle TA6L8 at NPR = 4 for (*a*,*c*) $m = 0$ mode at $St = 0.354$ and (*b*,*d*) $m = 1$ mode at $St = 0.283$. (*a*,*b*) Real component of ϕ and (*c*,*d*) absolute value of ϕ. Here, ϕ was normalised by its maximum value.

as per Nekkanti & Schmidt (2021) reveals that it results from the slight unsteadiness in the peak frequency and, hence, will not be further discussed. A convergence study was performed to ensure that the SPOD results are independent of the number of samples used in the analysis. Details of the study and the time–frequency analysis can be found in Appendix A.

The mode shapes (ϕ) associated with these peaks are shown in figure 6 with the real and absolute values for the $St = 0.354$ peak in figure 6(*a*,*c*) and the $St = 0.283$ peak in figure 6(*b*,*d*). In general, both modes exhibit standing-wave patterns in the axial direction, which indicates the presence of opposite-travelling waves – a common feature of resonance in screeching jets (Westley & Woolley 1975; Panda 1999; Edgington-Mitchell *et al.* 2022). From the real component of ϕ, it can be seen that the former is symmetric across the centreline, representing an $m = 0$ mode, while the latter manifests as an antisymmetric mode. Another feature that distinguishes these modes is the location of the peaks in the SPOD mode, where the peaks for the $m = 1$ mode are located further downstream and distributed more broadly in the axial domain (figure 6*d*) compared with the $m = 0$ mode (figure 6*c*). This difference in peak-amplitude location suggests that these two modes might involve triadic interaction between the KH wavepacket and different regions of quasi-periodicity in the mean flow. It should be noted that the assignment of the SPOD modes to the specific azimuthal wavenumbers (i.e. $m = 0$ or $m = 1$) relies on the observed symmetry of the real component of the projected mode shape. Because SPOD analysis was performed on two-dimensional path-integrated schlieren images, rather than a fully three-dimensional field or azimuthally decomposed data, this identification remains inferential. Specifically, it is strictly infeasible to distinguish between the $m = 0$ mode and higher-order symmetric modes (i.e. $m = 2, 4, \ldots$) or between the $m = 1$ mode and higher-order antisymmetric modes (i.e. $m = 3, 5, \ldots$). Nevertheless, the assignment of the SPOD modes to $m = 0$ and $m = 1$ modes is justifiable considering that dominant flow dynamics of FSS can be captured with $m = 0$ and $m = 1$ azimuthal modes (Baars *et al.* 2012) and the agreement with LSA results conducted using these wavenumbers as discussed in § 3.2.

To gain better insight into the waves that are involved in these coherent structures, a streamwise Fourier transform was performed on SPOD modes at the resonant frequencies to obtain the wavenumber spectra, which are shown in figure 7. Here, the positive wavenumbers indicate the coherent structures with positive (downstream) phase speed and

https://doi.org/10.1017/jfm.2026.12185 Published online by Cambridge University Press

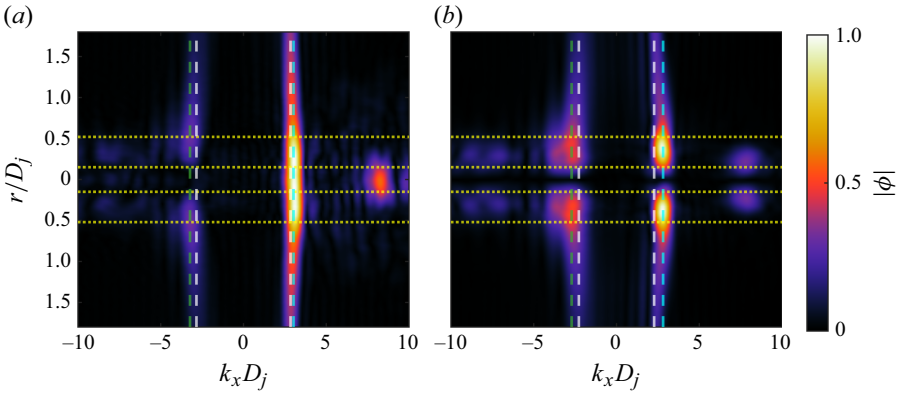


Figure 7. Wavenumber spectra of nozzle TA6L8 at NPR = 4 for (*a*) $m = 0$ mode and (*b*) $m = 1$ mode. White dashed lines: sonic wavenumber; cyan dashed line: wavenumber of the downstream peak; green dashed line: wavenumber of the upstream peak; yellow dotted line: radial positions of the inner and outer shear layers.

negative wavenumbers for negative (upstream) phase speed. For both $m = 0$ and $m = 1$ modes, there are energy peaks in both positive- and negative-wavenumber regions. To separately obtain the mode shapes of these peaks in physical space, their local wavenumber spectra were isolated by applying rectangular filters centred at the peak locations. It should be noted that the width of these filters is essentially subjective, and has been selected here essentially by visual inspection of the wavenumber spectra. The results are sensitive to the width of this filter, but here the bandwidth of the filter is sufficiently large that small changes do not greatly influence the result. This argument is justified by a sensitivity analysis, which can be found in Appendix B along with the details of the window size used in this study. The resulting spectra were then inverse Fourier transformed. Figure 8 illustrates the outcome of this process, with the left-hand column presenting the isolated wavenumber spectra and the right-hand column providing the associated mode shapes. There are other peaks manifest in the spectra with positive phase velocity and a wavenumber range of $kD_j \approx [6, 9]$ in both azimuthal modes. These peaks can be associated with the downstream-travelling duct mode (Edgington-Mitchell *et al.* 2021), or the KH wavepacket modulation caused by the shock structure (Nogueira *et al.* 2022*c*). Since these peaks are not relevant to the present study, they will not be further discussed.

The downstream-travelling wave, as shown in figures 7 and 8(*d*,*h*), has a subsonic phase speed and significant energy content in the radial locations associated with the supersonic annulus where the shear layers of the jet are situated, for both azimuthal modes. It also exhibits a spatially growing behaviour reaching a maximum amplitude in the region from the third to the fifth shock cell, followed by a decay further downstream, with only small axial wavenumber variation across the domain. These behaviours are entirely consistent with the characteristics of the KH wave, which arises from the inviscid shear-layer instability of the jet. As discussed, the KH wave plays a crucial role in sustaining screech resonance as it is responsible for supplying the energy to the resonance loop (Edgington-Mitchell 2019).

Shifting to the upstream-propagating wave, similar features are shared by both azimuthal modes. Generally, this wave has a subsonic phase speed and exhibits a much lower energy content compared with the downstream-travelling wave. Its energy peak is located in the supersonic annulus region of the jet, followed by an exponential decay in the quiescent

https://doi.org/10.1017/jfm.2026.12185 Published online by Cambridge University Press

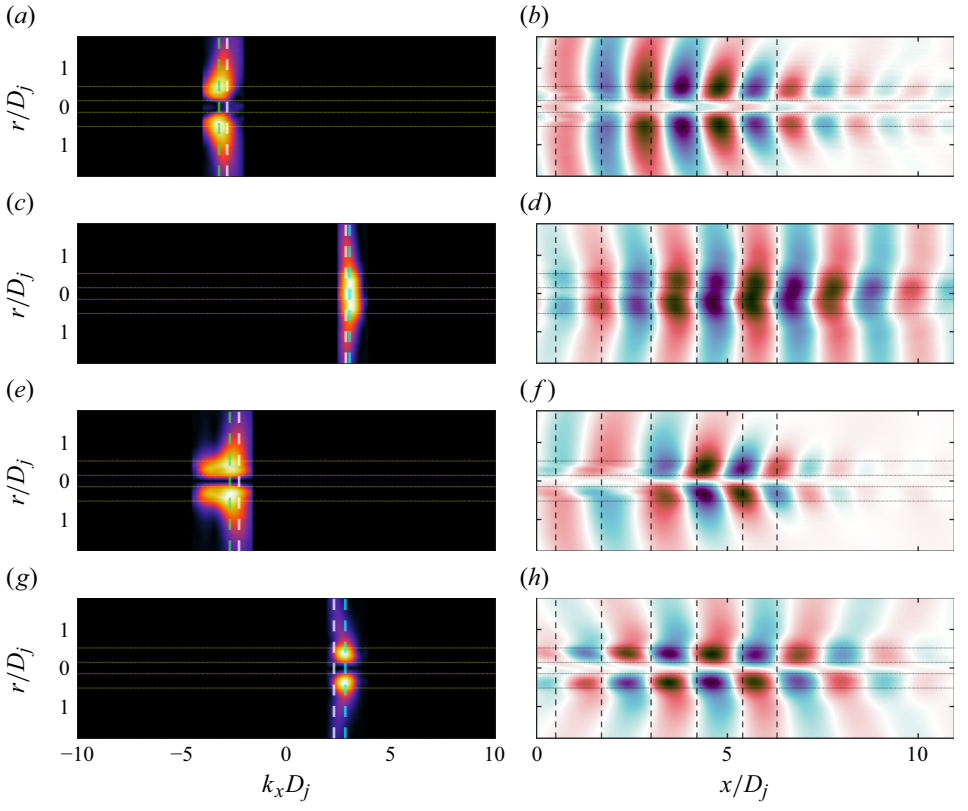


Figure 8. Isolated wavenumber spectra of the upstream- and downstream-travelling waves (*a*,*c*,*e*,*g*) and their associated mode shapes (*b*,*d*,*f*,*h*) of nozzle TA6L8 at NPR = 4. (*a*,*b*,*c*,*d*) The $m = 0$ mode and (*e*,*f*,*g*,*h*) the $m = 1$ mode. White dashed lines: sonic wavenumber; cyan dashed line: wavenumber of the downstream peak; green dashed line: wavenumber of the upstream peak; black vertical dashed line: location of normal shocks located aft of the Mach disk in the jet core; black and yellow horizontal dotted line: location of the inner and outer shear layers.

region (depicted in figures 7 and 8*b*,*f*). Notably, this wave possesses radial support in the domain both inside and outside the jet. The observed features align closely with the signatures of the GJM reported in past studies (Tam & Hu 1989; Edgington-Mitchell *et al.* 2021; Nogueira *et al.* 2024). These results provide evidence that the downstream-propagating and upstream-propagating waves in these modes are the KH and GJM waves, respectively.

In summary, from the experimental observations, two energetic modes have been identified for nozzle TA6L8 at NPR = 4, with one associated with the $m = 0$ azimuthal mode and the other with the $m = 1$ azimuthal mode. The $m = 1$ mode was found to be significantly more energetic than the $m = 0$ mode. The SPOD analysis reveals that there are two opposite-travelling waves that exist in these coherent structures. The downstream- and upstream-travelling waves exhibit features that are consistent with the signatures of the KH and GJM waves, respectively, which are the key ingredients of a screech resonance loop (Edgington-Mitchell *et al.* 2022). This finding is consistent with Bakulu *et al.* (2021) and serves as strong evidence for the hypothesis that screech does exist in the FSS pattern. To consolidate this argument, LSA was performed to further characterise these waves, which is discussed in the next section.

https://doi.org/10.1017/jfm.2026.12185 Published online by Cambridge University Press

3.2. *Linear modelling evidence*

From experimental observations, two opposite-travelling waves have been identified at a single frequency, whose structures are consistent with a KH wavepacket and a GJM. In this section, we use linear stability theory to confirm that these are in fact the aforementioned waves; LSA only predicts a finite set of waves that can be present in these flows, all of which are now relatively well understood (Jordan *et al.* 2018; Nogueira *et al.* 2024). The method requires smooth mean-flow profiles (as to avoid the appearance of spurious modes); hence, the mean-flow profiles were treated to smooth out discontinuities and wiggles induced by the shocks. The approach was based on fitting continuous analytical functions to the flow-variable radial profiles at certain streamwise positions and performing the analysis on them rather than the original RANS data. Considering the similarities between a coaxial-jet radial profile and that of the FSS mean flow, the analytical profile proposed by Perrault-Joncas & Maslowe (2008), with some modifications, was used for the fitting processes. The base flow quantities may then be written as

$$\begin{aligned} U(r) =& (1-h_u)\left\{\frac{w_{u1}}{2}\left[1+\tanh\left[b_{u1}\left(\frac{R_{u1}}{r}-\frac{r}{R_{u1}}\right)\right]\right]\right\} \\ &+ h_u\left\{\frac{w_{u2}}{2}\left[1+\tanh\left[b_{u2}\left(\frac{R_{u2}}{r}-\frac{r}{R_{u2}}\right)\right]\right]\right\}, \end{aligned} \tag{3.1}$$

$$\begin{aligned} \frac{1}{\nu}(r) =& \left\{(1-h_\nu)\left[\frac{w_{\nu1}}{2}\left[1+\tanh\left[b_{\nu1}\left(\frac{R_{\nu1}}{r}-\frac{r}{R_{\nu1}}\right)\right]\right]\right]\right. \\ &\left.+ h_\nu\left[\frac{w_{\nu2}}{2}\left[1+\tanh\left[b_{\nu2}\left(\frac{R_{\nu2}}{r}-\frac{r}{R_{\nu2}}\right)\right]\right]\right]\right\}+1, \end{aligned} \tag{3.2}$$

$$\begin{aligned} P(r) =& \left\{\frac{h_{p1}}{2}\left[1+\tanh\left[b_{p1}\left(\frac{R_{p1}}{r}-\frac{r}{R_{p1}}\right)\right]\right]\right. \\ &\left.+\frac{h_{p2}}{2}\left[1+\tanh\left[b_{p2}\left(\frac{R_{p2}}{r}-\frac{r}{R_{p2}}\right)\right]\right]\right\}+1. \end{aligned} \tag{3.3}$$

Here, in each equation, the subscripts 1 and 2 represent the properties of the inner and outer shear layers, respectively, R is the radial location of the shear layer, b governs the radial gradient of fluid variables at the shear layer and h controls the ratio between the properties of the outer and inner jets (see Gloor *et al.* (2013) for details). Additional weighting factors, w, were introduced to provide more flexibility for the fitting process. In this process, radial grid r and RANS data were supplied as inputs and $[R, b, h, w]$ were the tuning parameters. The fitting was conducted using the nonlinear least-squares method via MATLAB's curve-fitting toolbox, resulting in R^2 values exceeding 0.97 for all variables. Figure 9 shows the fitted mean-flow profiles and their first derivative for nozzle TA6L8 at NPR = 4, $x/D_j \approx 0$ (mean-flow data were linearly interpolated from the closest RANS grid points to the nozzle exit). This axial location was selected arbitrarily to demonstrate the fitting process and LSA results. It can be observed that the analytical profiles fit the RANS data well and also mitigate wiggles, which leads to smooth and continuous first-derivative profiles. For the current case, LSA was performed for a streamwise range of $x/D_j = [-0.4 : 6]$ with $\Delta x/D_j = 0.1$. The justification for this range is discussed later in this section.

https://doi.org/10.1017/jfm.2026.12185 Published online by Cambridge University Press

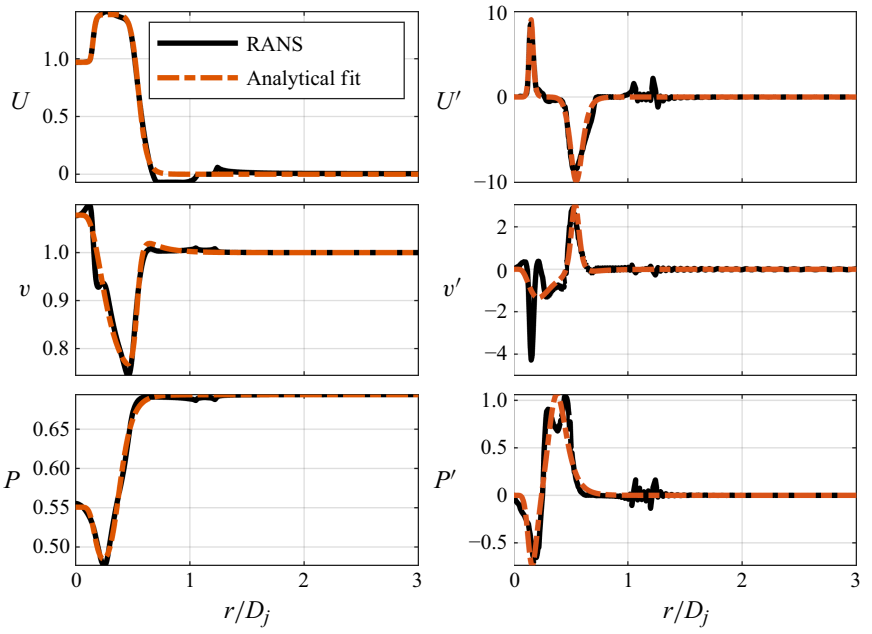


Figure 9. Nozzle TA6L8 NPR = 4 analytically fitted mean-flow profiles at $x/D_j \approx 0$.

With confidence in the fitting process, LSA was performed on the fitted profiles for multiple axial locations. The LSA spectrum for $St = 0.25$ at the exit plane of nozzle TA6L8 operating at NPR = 4 is shown in figure 10. Here, the horizontal (real) axis represents the spatial wavenumber and the vertical (imaginary) axis determines the growth rate of each mode as previously discussed in § 2.3. Again, the positive wavenumber indicates a positive phase velocity, and the negative wavenumber indicates a negative phase velocity. For both azimuthal modes, there are similarities between the two spectra with the flow profile supporting KH, GJM, duct, acoustic and critical-layer wave modes (Towne *et al.* 2017). The KH instability waves manifest in the spectra as two separate modes, inner (red circle) and outer KH (red square), which are associated with the inner and outer shear layers of the jet, respectively. In the negative-wavenumber region, the GJM (red triangle) manifests in the spectra as a discrete mode with a slight subsonic phase velocity. Its eigenvalue lies on the real axis, highlighting the neutral nature of this wave. After identifying the supported modes, the next part of this section will focus on a detailed study of the characteristics of these waves for the current flow case.

Starting with the KH wave, the spectra of the modes associated with this wave are presented in figure 11 for the frequency range $St = [0.2 : 0.5]$ with $\Delta St = 0.005$ at the exit plane of nozzle TA6L8 operating at NPR = 4. It can be observed that both the inner and outer KH modes are supported by the flow for a wide range of frequencies. For both azimuthal modes, the outer KH mode possesses a subsonic phase velocity, while the inner KH has a supersonic phase velocity compared with the ambient speed of sound. The former also exhibits a higher growth rate for the entire frequency domain, which can be explained by the higher velocity gradient of the outer shear layer, as shown in figure 9. These findings are consistent with the recent work of Jaunet & Lehnasch (2025).

Figure 12 shows the radial profiles of the pressure fluctuation associated with the KH waves. In general, the main difference between the two azimuthal modes is that for the

https://doi.org/10.1017/jfm.2026.12185 Published online by Cambridge University Press

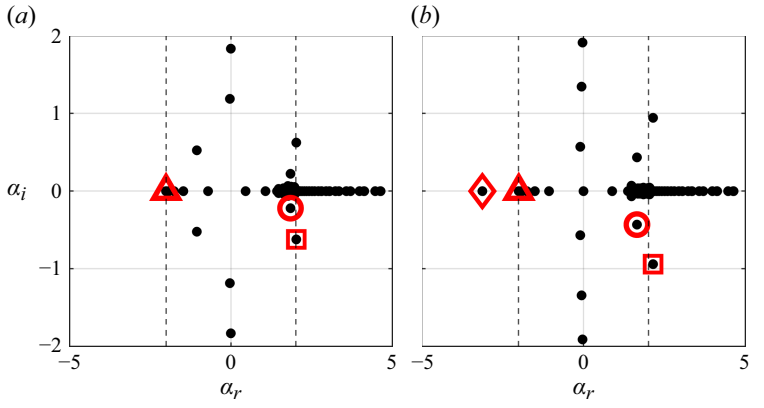


Figure 10. The LSA spectra at $x/D_j \approx 0$, $St = 0.25$ of nozzle TA6L8 NPR = 4 for (*a*) $m = 0$ mode and (*b*) $m = 1$ mode. Red circle: inner KH mode; red square: outer KH mode; red triangle: GJM; red diamond: duct mode; black dashed line: sonic line.

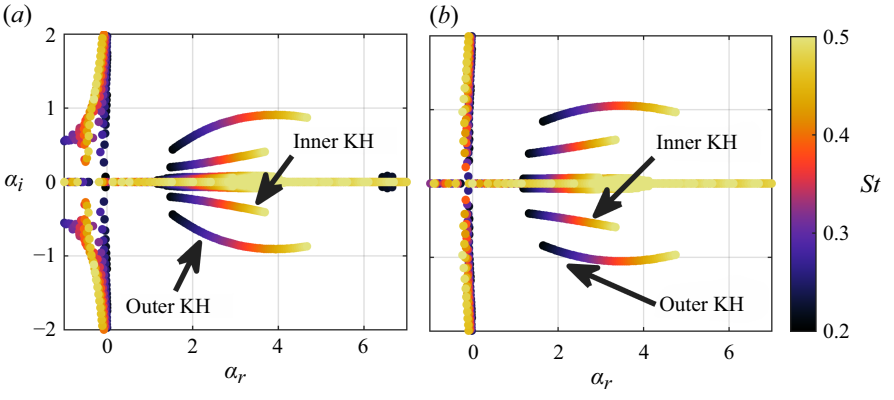


Figure 11. The KH spectra of nozzle TA6L8 NPR = 4 at $x/D_j \approx 0$, $St = 0.25$ for (*a*) $m = 0$ mode and (*b*) $m = 1$ mode.

$m = 0$ KH modes, the pressure perturbation possesses a magnitude at the centreline, whereas for $m = 1$ modes, the pressure fluctuation is zero at this location, consistent with the boundary conditions applied in the LSA. Both inner and outer KH waves manifest peaks at the areas corresponding to the shear layers, followed by a rapid decay in the quiescent region. This trend is similar to that observed in the SPOD modes discussed in § 3.1, where the KH wave peaks were found to be confined in the supersonic annulus region. The inner KH wave possesses a consistent radial shape for the whole studied St range with its primary peak located at the jet inner shear layer ($r/D_j \approx 0.15$) and a smaller peak at the outer shear layer ($r/D_j \approx 0.57$). On the other hand, the outer KH wave shows variation in its radial structure as the frequency changes. At lower frequencies ($St < 0.3$), this mode has two prominent peaks associated with the inner and outer shear layers. As the frequency increases, the magnitude of the inner-shear-layer peak diminishes, leaving the outer-shear-layer peak as the dominant one. The main reason for the existence of the inner peak in the outer KH radial profile and vice versa is that at low frequency, the structure of the inner and outer KH waves is mixed together as shown in Gloor *et al.*

https://doi.org/10.1017/jfm.2026.12185 Published online by Cambridge University Press

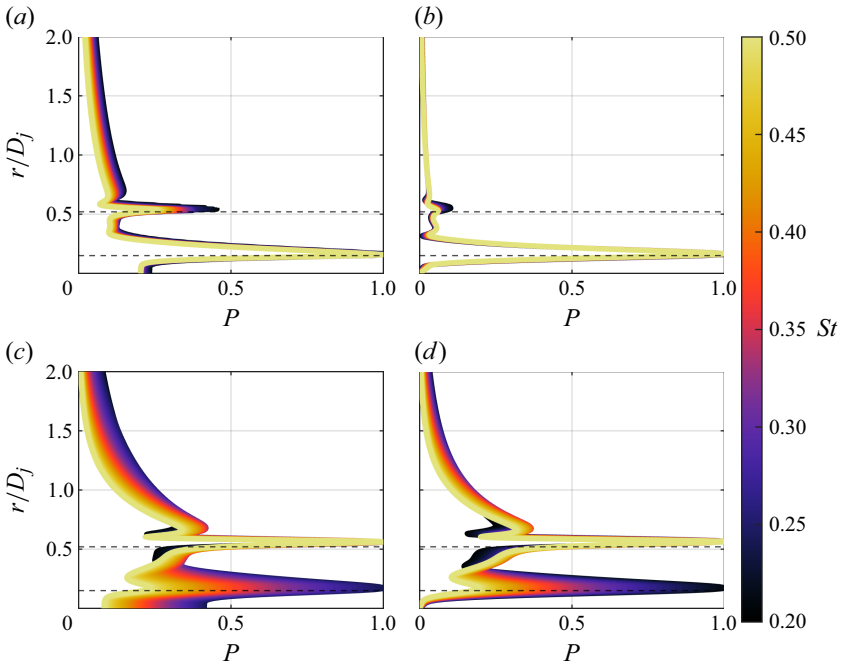


Figure 12. Eigenfunctions of pressure fluctuation of KH waves of nozzle TA6L8 NPR = 4. (*a*) Inner KH for $m = 0$ mode, (*b*) inner KH for $m = 1$ mode, (*c*) outer KH for $m = 0$ mode and (*d*) outer KH for $m = 1$ mode. Horizontal dashed line: location of the inner and outer shear layers. Eigenfunctions were normalised by their maximum values.

(2013). Another difference between the outer and inner KH waves is that the former has more radial support by the flow with an additional peak outside of the jet ($r/D_j \approx 0.68$). However, this behaviour is in contrast with the finding of Jaunet & Lehnasch (2025) where the authors reported that the inner KH wave had more radial support outside of the jet compared with the outer KH wave. These differences could be from either the choice of mean flow (Gloor *et al.* 2013) or the governing equations employed (i.e. the linearised Navier–Stokes or compressible Rayleigh equations), which are known to affect the mode shapes.

The GJM is identified in the spectra as a discrete mode on the real axis with a slight subsonic phase velocity in the negative-wavenumber domain. Unlike the KH modes, the GJM is only supported in a narrow frequency range. Its signature in the spectra is demonstrated in figure 13. As a discrete mode, the GJM detaches from the continuous acoustic branch at the branch point ($St = 0.250$, figure 13*a*). As the frequency increases, it continues to move in the negative direction ($St = 0.260$, figure 13*b*) until it collides with the duct mode ($St = 0.265$, figure 13*c*) at the saddle point, resulting in an evanescent wave ($St = 0.275$, figure 13*d*). Hence, the branch and saddle points indicate the cuton and cutoff frequencies at which the neutral GJM can be supported by the flow.

The pressure perturbation profiles of the GJM are illustrated in figure 14. It can be seen that the GJM is supported by the flow in different frequency bands for the two azimuthal modes, with a higher range for the $m = 0$ mode. Also, for these two azimuthal wavenumbers, the GJM possesses different radial orders. For the $m = 0$ mode, the GJM has a second-order radial structure with two peaks in the profile, with the primary one located at the jet centreline and the secondary one located close to the outer shear layer.

https://doi.org/10.1017/jfm.2026.12185 Published online by Cambridge University Press

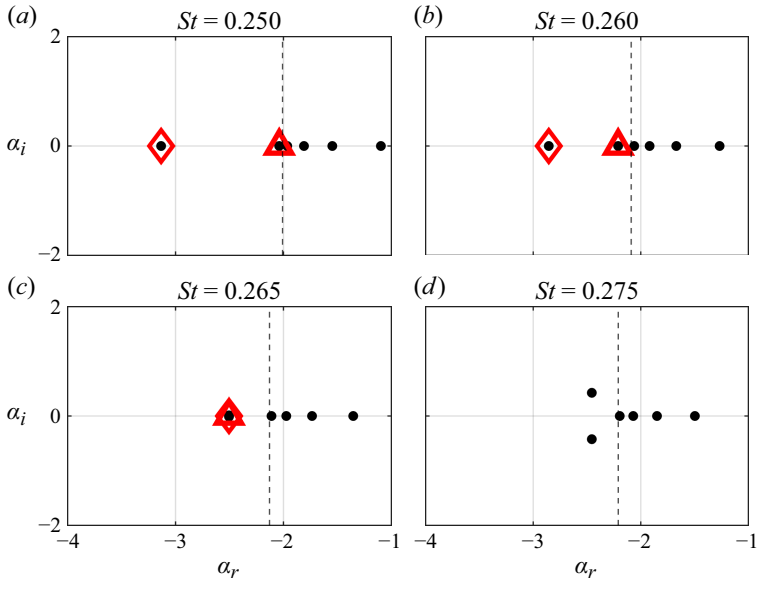


Figure 13. (*a–d*) The evolution of the GJM for nozzle TA6L8 NPR = 4, $m = 1$ mode at $x/D_j = 4$. Red triangle: GJM; red diamond: duct mode; black dashed line: sonic line.

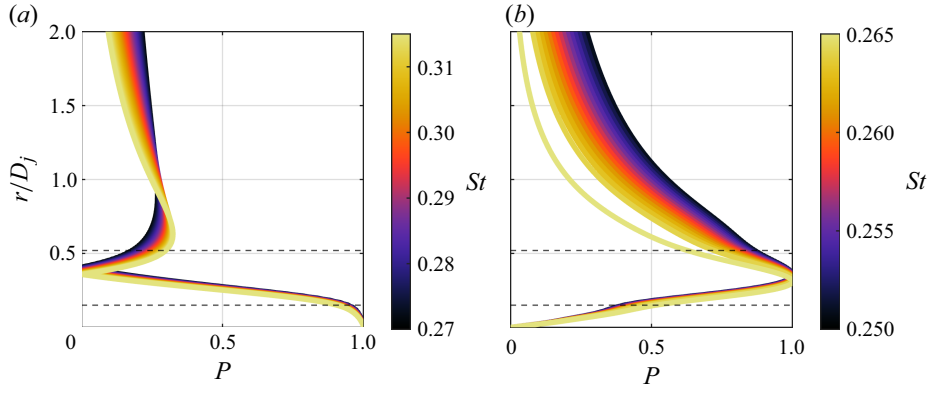


Figure 14. Eigenfunctions of pressure fluctuation of GJM of nozzle TA6L8 NPR = 4 at $x/D_j = 4$: (*a*) $m = 0$ mode and (*b*) $m = 1$ mode. Horizontal dashed line: location of the inner and outer shear layers. Eigenfunctions were normalised by their maximum values.

For the $m = 1$ mode, a first radial order is observed, with a single peak located between two shear layers. Both are followed by an exponential decay in the far field with more rapid decay rates as St increases. Unlike KH waves, the GJM possesses more radial support in the quiescent region. While the wave clearly has negative phase velocity, it is necessary to demonstrate that it also has negative group velocity ($\partial\omega/\partial k$) to prove that it is carrying energy upstream. According to the Briggs–Bers criterion (Briggs 1964), positive group velocity ($\partial\omega/\partial k > 0$) denotes downstream propagation and negative group velocity ($\partial\omega/\partial k < 0$) denotes upstream propagation. The dispersion relation of the GJM waves is shown in figure 15, where the dispersion relation of the downstream-travelling duct mode

https://doi.org/10.1017/jfm.2026.12185 Published online by Cambridge University Press

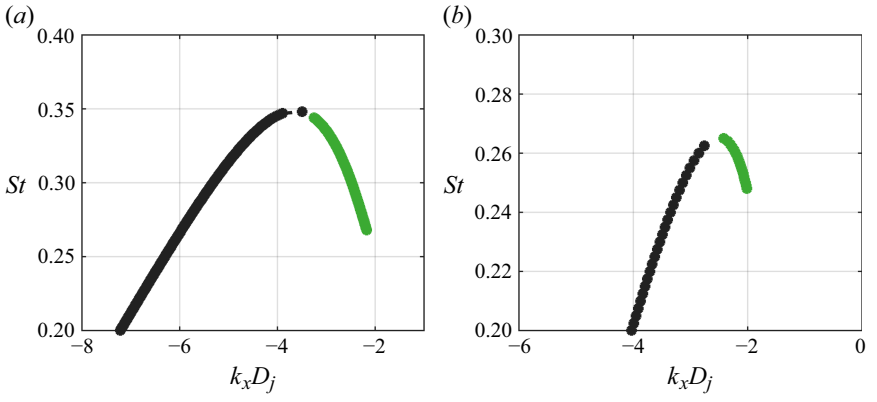


Figure 15. Dispersion relation of the GJM of nozzle TA6L8 NPR = 4 at $x/D_j = 4$: (*a*) $m = 0$ mode and (*b*) $m = 1$ mode. Green curve: GJM; black curve: duct mode.

is also included for completeness. Here, as the frequency increases, the wavenumber of the GJM becomes more negative for both azimuthal modes, which leads to a negative group velocity, confirming that this wave carries energy in the upstream direction and hence can close the resonance loop.

With the KH waves and GJM characterised, we now refer back to the experimental observations to confirm if these LSA modes are indeed the waves identified from SPOD as discussed in § 3.1. To do so, their wavenumbers at the resonant frequencies obtained from both methods will be compared. For the experimental data, radial averaging was performed on the wavenumber spectra (figure 7) within the jet region ($r/D_j = [-0.5 : 0.5]$). The wavenumbers corresponding to the KH and GJM waves were then identified from the primary peaks in the positive- and negative-wavenumber domains of the averaged spectra, respectively. For the LSA results, the approaches to obtain the wavenumbers of KH and GJM waves are slightly different. For the KH waves, their wavenumbers were extracted and averaged over the first shock cell $x/D_j = [-0.4 : 0.1]$ (the region located aft of the Mach disk and the triple point). Taking advantage of the slow axial-wavenumber variation across the domain, these averaged values were assumed to be constant downstream. The selection of this region – around the location where the shear layers start – is justified by the fact that LSA can accurately predict the growth behaviour of disturbances in this regime, as demonstrated in Cavalieri *et al.* (2013). For the GJM, the averaged wavenumber values were obtained from the flow region where the peaks were found in the SPOD modes (see figure 6), as these waves are generated further downstream. For example, for the $m = 1$ resonance, the averaged GJM wavenumber was calculated in the domain $x/D_j = [2 : 6]$ (see figure 6*d*).

Figure 16 and table 3 show the comparison between LSA and SPOD wavenumbers. Here, k_u and k_d represent the upstream and downstream peak wavenumbers. For LSA, k_{KH} and k_{GJM} represent the wavenumbers of the KH and GJM waves, with the subscripts i and o indicating inner and outer shear layers, respectively. For both resonance modes, there is agreement between the wavenumbers obtained from the two methods. The GJM wavenumber shows a good match with an absolute error of around 7 %. In the case of the KH wave, a notable feature is that for the $m = 0$ resonance, the downstream SPOD peak aligns with the LSA k_{KH_i}, while for the $m = 1$ resonance, it aligns with k_{KH_o}. While this could suggest that different KH waves are responsible for closing different screech loops, the proximity between the wavenumbers and the inherent limitations of the locally parallel

https://doi.org/10.1017/jfm.2026.12185 Published online by Cambridge University Press

	$m=0$			$m=1$		
SPOD	k_d		k_u	k_d		k_u
	3.13		−3.23	2.81		−2.61
LSA	k_{KH_i}	k_{KH_o}	k_{GJM}	k_{KH_i}	k_{KH_o}	k_{GJM}
	3.01	3.53	−3.00	3.13	2.77	−2.44
Error (%)	−3.83	12.78	−7.12	11.39	−1.42	−6.51

Table 3. Comparison between SPOD peak wavenumbers and LSA mean wavenumber predictions.

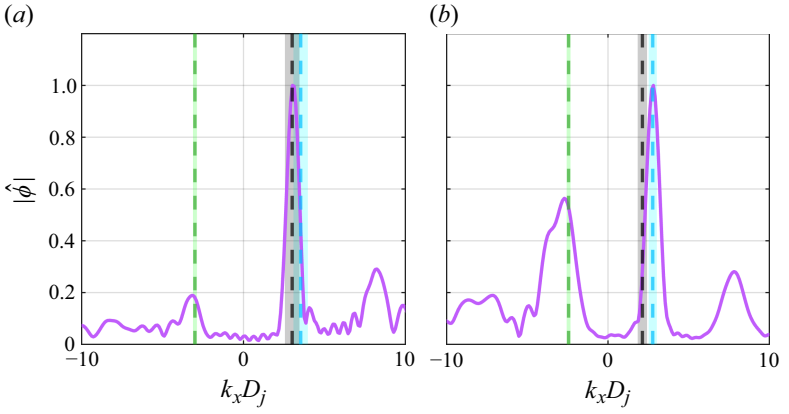


Figure 16. Wavenumber comparison between LSA and SPOD of nozzle TA6L8 NPR = 4 at $x/D_j = 4$: (*a*) $m = 0$ mode and (*b*): $m = 1$ mode. Black dashed line: LSA inner KH wavenumber; cyan dashed line: LSA outer KH wavenumber; green dashed line: LSA GJM wavenumber; purple solid line: averaged SPOD wavenumber spectrum; shaded area: standard deviation of the LSA wavenumbers.

approach hinder the identification of the KH mode responsible for resonance if based on a wavenumber comparison alone. In general, the agreement between LSA and experimental results serves as strong evidence that the KH waves and GJM found to be supported by the flow from LSA are indeed the two opposite-travelling waves found in the SPOD modes. This is a crucial finding as these waves are the key ingredients of a screech resonance loop. The discovery of these waves here strengthens the hypothesis that screech does exist in the FSS regime. Further evidence for the phenomenon can be obtained by evaluating whether the experimental resonant frequencies can be accurately predicted using STIM. This is performed in the next section.

3.3. *The STIM predictions*

With the wavenumbers of the KH waves and the GJM obtained and validated from LSA, STIM is now employed to predict the resonant frequencies. As discussed in § 2.4, the implementation of this model requires the wavenumbers of the KH waves (k_{KH}), the GJM (k_{GJM}) and also the wavenumber of the shock structure (k_{sh}) where the interaction between the KH wavepacket and the shock-cell structure occurs. In the work of Edgington-Mitchell *et al.* (2022), it has been demonstrated that this wavenumber can be obtained from the standing-wave pattern observed from the SPOD mode (k_{sw}). By performing an axial Fourier transform on the standing-wave region of the SPOD mode, k_{sw} is identified as the primary peak from the resulting wavenumber spectra.

https://doi.org/10.1017/jfm.2026.12185 Published online by Cambridge University Press

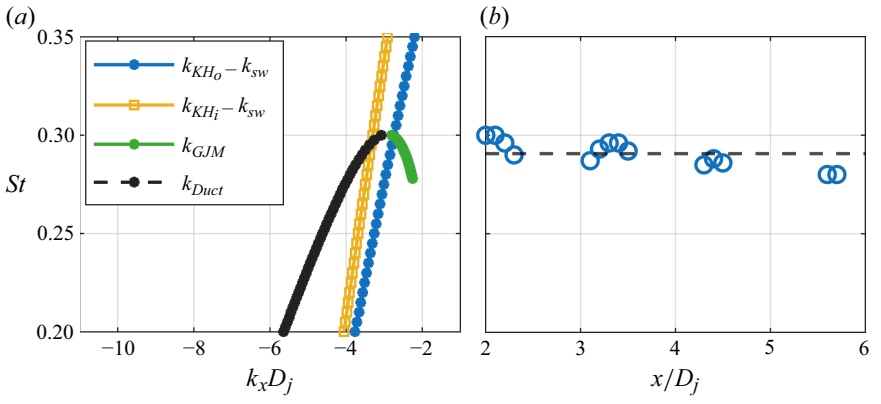


Figure 17. (*a*) The STIM prediction of nozzle TA6L8 NPR = 4 at $x/D_j = 3.3$. (*b*) The STIM predictions for this case at $x/D_j = [2:6]$.

After obtaining all of the required inputs, STIM was applied to predict the resonant frequencies. The predictions for nozzle TA6L8 at NPR = 4 and $m = 1$ are shown in figure 17. Figure 17(*a*) illustrates the prediction method at $x/D_j = 3.3$. As alluded to earlier, the predicted frequency of STIM is the frequency at which k_{KH}, k_{GJM} and k_{sw} satisfy (1.2). In other words, it is the frequency at which the intersection between the k_{GJM} and $k_{KH_o} - k_{sw}$ (outer KH) or $k_{KH_i} - k_{sw}$ (inner KH) curves occurs. Hence, in this case, $St = 0.299$ is the predicted resonant frequency. The same procedure was repeated across the range $x/D_j = [2:6]$, where the spatial peaks were observed in the SPOD mode of this resonance, using the local GJM wavenumber and the KH wavenumber obtained around the first shock cell (as the KH becomes stable in that region). The outcomes for this process are demonstrated in figure 17(*b*). It can be seen that there are slight variations in the predicted frequencies between different axial locations. This is because variations in the mean-flow profiles along the axial location lead to the slight differences in the k_{GJM} computed by LSA; since constant values of k_{sw} and k_{KH} were assumed, the changes in k_{GJM} directly affect the predicted frequencies. However, the predictions are still close to the resonant frequency observed in the experiment, represented by the dashed line in figure 17(*b*). The final predicted frequency was taken as the average of all the predictions within this range, resulting in a value of $St = 0.291$, which has an error of 2.83 % compared with the experimental value of $St = 0.283$. The same analysis was performed for the $m = 0$ resonance, and the outcomes for both resonance modes are summarised in table 4. For the $m = 0$ case, two predictions were obtained corresponding to the two KH waves, as both of them intersect with the k_{GJM} curve within the supported frequency range. Again, due to the proximity between the two predicted frequencies, it is impossible to discern which KH is responsible for closing the resonance loop in this case. In the STIM framework, as long as (1.2) is satisfied, the flow condition permits the screech loop to occur (Edgington-Mitchell *et al.* 2022). Evidently, the predictions from both azimuthal modes agree well with the experimental values with errors of less than 4 %.

Following the successful predictions of the resonant frequencies for nozzle TA6L8 at NPR = 4, the above procedure was repeated for other operating conditions. The waterfall spectrum combining the SPOD spectra for all NPR cases of nozzle TA6L8 is shown in figure 18. The Tam *et al.* (1986) semi-empirical screech model is also included (white dashed curve) for clarity. In this figure, the vertical dashed lines indicate the NPRs at which RANS simulations were computed. The predictions from STIM for both azimuthal modes

https://doi.org/10.1017/jfm.2026.12185 Published online by Cambridge University Press

m	Type	St (SPOD)	St (LSA)	Error (%)
0	Outer KH	0.354	0.341	3.67
0	Inner KH	0.354	0.361	1.98
1	Outer KH	0.283	0.291	2.83

Table 4. The STIM predictions for nozzle TA6L8 at NPR = 4.

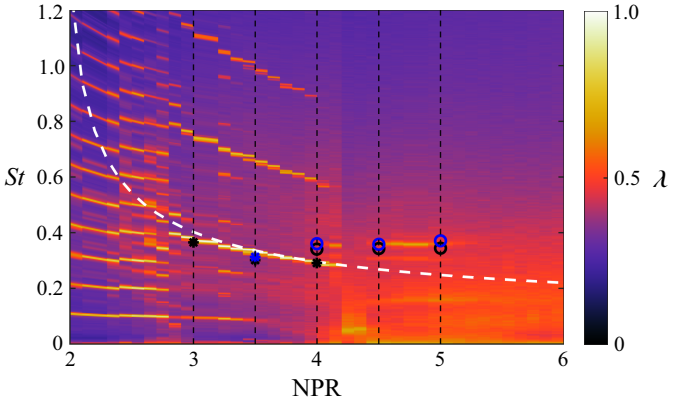


Figure 18. Spectrogram for nozzle TA6L8. Black markers: predictions associated with the outer KH; blue markers: predictions associated with the inner KH; circle markers: $m = 0$ predictions; star markers: $m = 1$ predictions; white curve: Tam's model; black vertical dashed line: NPRs at which RANS simulations were conducted. Data were normalised by the maximum value and rescaled. Schlieren and RANS mean fields, SPOD spectra and mode shapes for all nozzles and NPRs can be accessed at https://www.cambridge.org/S0022112026121855/JFM-Notebooks/Figure18.ipynb.

are plotted as markers. Firstly, the experimental results demonstrate distinct resonance branches for both azimuthal modes across different NPR ranges. The branch associated with $m = 1$ resonance aligns well with the Tam curve from NPR = 2.7 to NPR = 4.3 before vanishing. The branch corresponding to $m = 0$ screech starts to appear close to where the $m = 1$ branch disappears and continues to NPR ≈ 5. There are also presented in figure 18 signatures of a different resonance loop at low NPRs < 3 with distinct SPOD mode shapes compared with a screech resonance loop. This could be attributed to transonic resonance (see Raman 1999) and will not be further discussed in this work. Besides the previously discussed NPR = 4 case, it can be seen that for NPRs = [3, 3.5], STIM captures well the resonant frequencies for the $m = 1$ branch and similarly for NPRs = [4.5, 5] for the $m = 0$ branch. For the cases where STIM cannot make a prediction, i.e. NPR = 4.5 for $m = 1$ and NPR = 3 for $m = 0$, this is because (1.2) was not satisfied for any frequency. Crucially, STIM was able to accurately predict all of the resonant frequencies observed in the experiments for both azimuthal modes, including the jump between $m = 1$ and $m = 0$ branches; furthermore, no prediction was obtained for the cases where no resonance was observed in the experiments. This is a significant finding because, as previously emphasised, STIM was designed to predict screech frequencies based on the triadic interaction framework. Therefore, the fact that all of the resonant frequencies observed in the experiments were accurately predicted by this model serves as strong evidence that screech is indeed present in the FSS regime, thereby confirming the hypothesis proposed by Jaunet *et al.* (2017).

https://doi.org/10.1017/jfm.2026.12185 Published online by Cambridge University Press

4. Screech loop behaviour as a function of nozzle design

Having confirmed that screech does exist in the FSS regime, we now focus on examining the screech loop behaviour in different nozzle contours. Figure 19 shows the spectrograms for other nozzles tested in this study, along with their STIM predictions. All the marker conventions are kept consistent with figure 18. Similar to the case of nozzle TA6L8, the RANS simulations were conducted on the NPRs indicated by the vertical dashed lines. Following the argument stated in § 3, it can be seen that screech manifests in all nozzles, as either an $m = 0$ or $m = 1$ azimuthal mode or both. There are some cases where multiple screech loops are experimentally observed with the same azimuthal wavenumber (for instance, TA2L15 at NPR $= 5$ for $m = 1$ mode; figure 19*f*). The predictions from STIM again agree well with experimental resonant frequencies for various nozzles. Again, for nozzles such as TA2L15 and TA4L8, there are also signatures of a different resonance loop at low NPR, similar to the case of TA6L8 and will not be further analysed.

The screech behaviour varies significantly between different nozzles. For some nozzles, such as TA2L15, screech exists in a wide and continuous NPR range for both azimuthal modes, while for some nozzles, such as TA4L8, screech only exists in a narrow NPR range and disappears. To explore the mechanisms that determine this behaviour, we start by examining the nozzles TA2L8 and TA2L15. From table 1, these two nozzles share the same exit area but have different divergence angles (18.5° and 10.1°, respectively). The reason for the selection of these nozzles for the analysis is that, despite sharing some dimensional similarities, they exhibit distinct screech behaviours as shown in figure 19(*c–f*). For nozzle TA2L8, screech only exists in a narrow NPR range (NPR $= 2.7$ to NPR $= 3.1$) for the $m = 1$ azimuthal mode, followed by an $m = 0$ screech branch at higher NPR and frequencies. As the NPR further increases, this branch then disappears (NPR ≈ 4.1) and the $m = 1$ branch reappears. In contrast, for nozzle TA2L15, screech for both azimuthal modes coexists in a wide and continuous NPR range (NPR $= 2.7$ to NPR $= 6$).

To shed light on the phenomenon, the flow structures of these two nozzles will be examined. Figure 20 shows the mean-flow fields obtained from experiments for nozzle TA2L8 (left-hand column) and TA2L15 (right-hand column) with the first, second and third rows corresponding to NPR $= 3$, NPR $= 4$ and NPR $= 5$, respectively. In general, the flow structures for both nozzles are similar for NPR $= 3$ with a pattern of shock diamonds. The differences arise at higher NPRs. For nozzle TA2L15, as the NPR ramps up, the shock-cell structure is stretched out and the shock wavelength increases. Other flow features do not exhibit significant changes; the shock-diamond structure retains its shape with the reflection point located at the jet centreline. In contrast, for nozzle TA2L8, there is a significant variation in the shock structure between NPR $= 3$ and NPR $= 4$, especially for the first few shock cells. At NPR $= 4$, it can be perceived that the Mach disk has enlarged, and a series of normal shocks emerges in the jet core. The shock-diamond structure is distorted in this case as the reflection points shift to the tips of these normal shocks. Further increases in NPR to 5 do not lead to substantial changes, just an increase in the shock-cell length. Recalling that the $m = 1$ screech branch for nozzle TA2L8 terminates at NPR ≈ 3.1, the drastic change in the shock structure between NPR $= 3$ and NPR $= 4$ might be the reason for this behaviour.

To elaborate this argument, RANS Mach number contours will be used to provide visualisation of the core structure of the flow. The Mach number contours for nozzle TA2L8 (left-hand column) and TA2L15 (right-hand column), at the same operating conditions as figure 20, can be seen in figure 21. The flow features observed in experiments are well captured by RANS. There are contrasting trends in the evolution of the shock-cell

https://doi.org/10.1017/jfm.2026.12185 Published online by Cambridge University Press

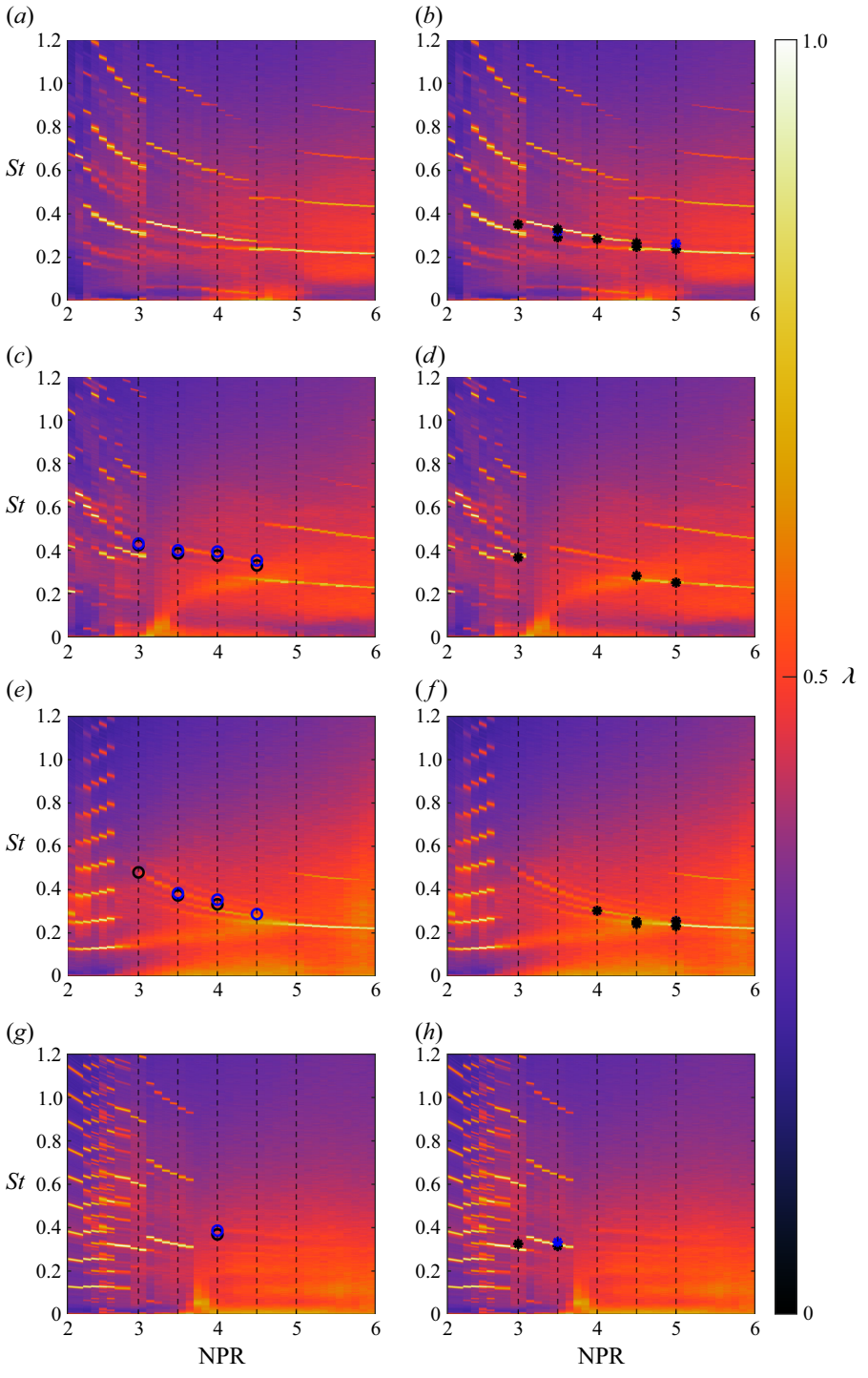


Figure 19. Spectrograms for nozzles (*a*,*b*) TA2L6, (*c*,*d*) TA2L8, (*e*,*f*) TA2L15 and (*g*,*h*) TA4L8. Black markers: predictions associated with the outer KH; blue markers: predictions associated with the inner KH; circle markers: $m = 0$ predictions (shown only in the left-hand column); star markers: $m = 1$ predictions (shown only in the right-hand column). Data were normalised by the maximum values and rescaled.

https://doi.org/10.1017/jfm.2026.12185 Published online by Cambridge University Press

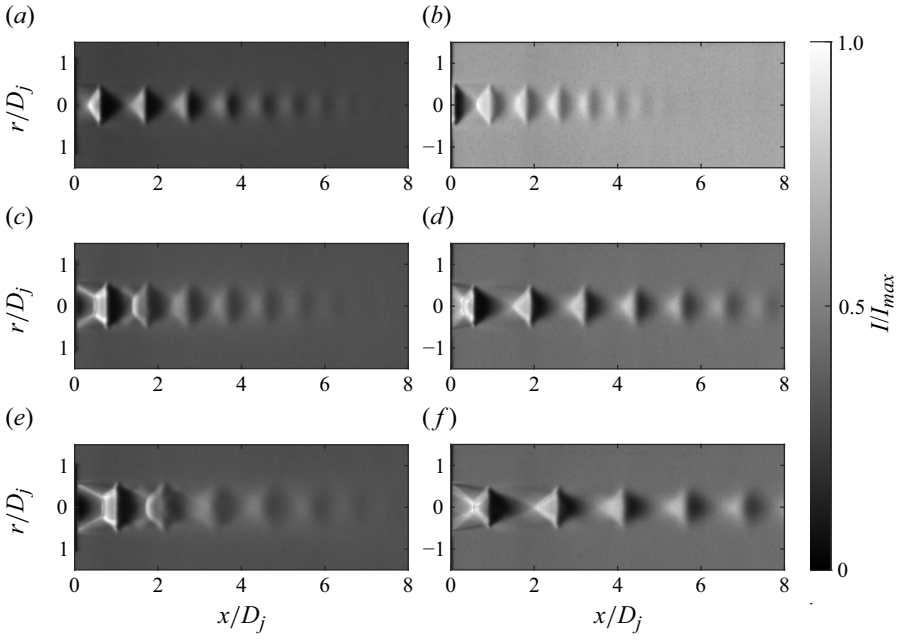


Figure 20. Mean schlieren images for nozzle TA2L8 (*a*,*c*,*e*) and nozzle TA2L15 (*b*,*d*,*f*), for (*a*,*b*) NPR = 3, (*c*,*d*) NPR = 4 and (*e*,*f*) NPR = 5.

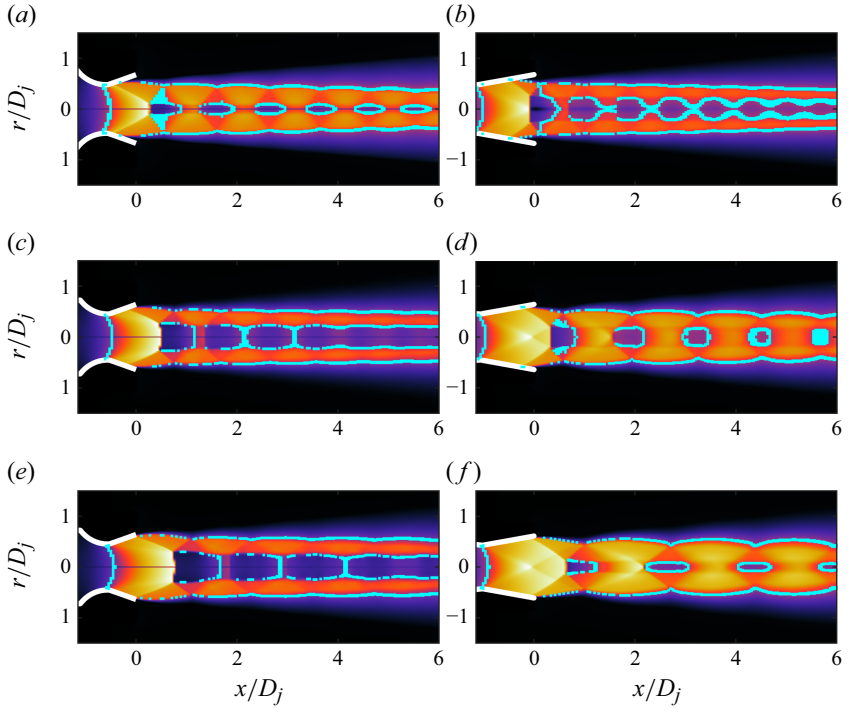


Figure 21. The RANS Mach number contours for nozzle TA2L8 (*a*,*c*,*e*) and nozzle TA2L15 (*b*,*d*,*f*), for (*a*,*b*) NPR = 3, (*c*,*d*) NPR = 4 and (*e*,*f*) NPR = 5. Cyan dotted curve: sonic line.

https://doi.org/10.1017/jfm.2026.12185 Published online by Cambridge University Press

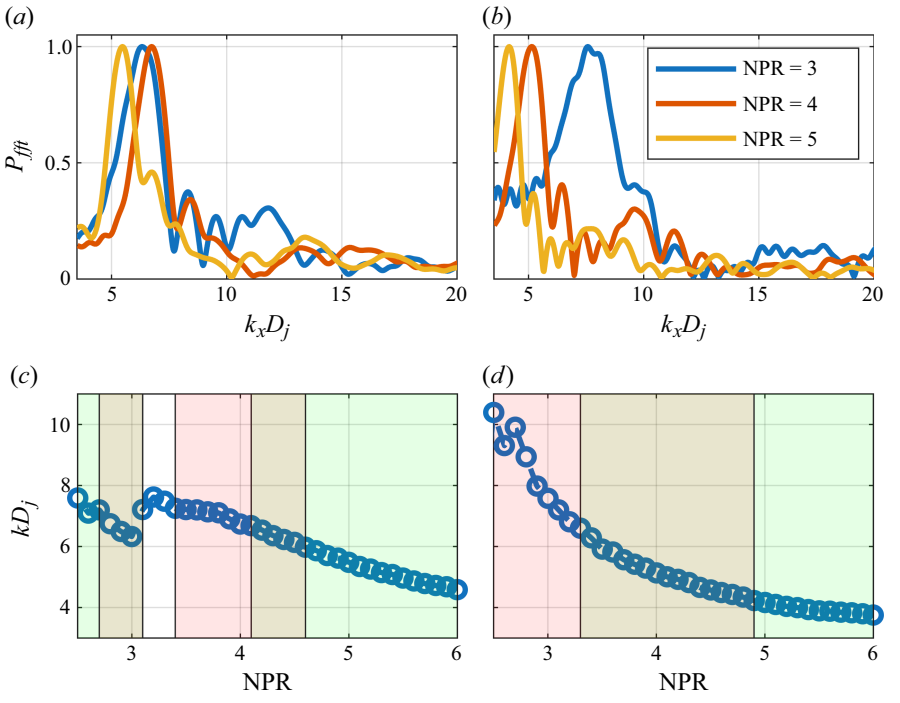


Figure 22. The Fourier transform of the centreline schlieren pixel intensities of (*a*) nozzle TA2L8 and (*b*) nozzle TA2L15. Shock-structure wavenumber (k_{sh}) of the primary peak for (*c*) nozzle TA2L8 and (*d*) nozzle TA2L15. Red shaded area: NPR range where $m = 0$ screech exists; green shaded area: NPR range where $m = 1$ screech exists; yellow shaded area: NPR range where both $m = 0$ and $m = 1$ screech exists.

structure for these two nozzles as NPR increases. Firstly, let us consider nozzle TA2L15. As NPR increases, the supersonic annulus radially expands, pushing the inner shear layer closer to the centreline while the Mach disk shrinks. The fact that the reflected shock inside this supersonic shear layer extends up to the jet centreline results in the shock-diamond structure observed for this nozzle in figure 20. Shifting to nozzle TA2L8, unlike nozzle TA2L15, the supersonic annulus gets thinner as NPR increases. Moreover, the Mach disk enlarges significantly, followed by a series of normal shocks with the tips of these shocks serving as the reflection points of the reflected shocks rather than the centreline. This explains the distortion of the shock-diamond structure observed in experiments.

To highlight the change in shock structure and its wavelength, an axial Fourier transform was performed on the mean schlieren field (figure 20) for both nozzles and the results are illustrated in figure 22. The wavenumbers of the shock-cell primary peak for these nozzles at all operating conditions are demonstrated in figures 22(*c*) and 22(*d*). For nozzle TA2L15, as discussed earlier, there is no significant variation in the mean-flow shock structure; the shock-cell wavenumber can be seen to decrease monotonically and continuously as NPR increases, at least in the range of NPR where screech is observed. In contrast, for nozzle TA2L8, a sudden jump in the wavenumber value can be observed at NPR = 3.1 followed by a gradual decrease at higher NPRs. This discontinuity in the primary wavenumber curve results in very different shock-cell wavenumbers throughout the NPR range, which can lead to changes in screech characteristics.

The changes in the shock-cell structure and wavenumber are crucial findings as they can explain the absence of screech or modal staging at certain NPRs for nozzle TA2L8. Referring back to the theoretical framework of the triadic interaction, screech can occur as

https://doi.org/10.1017/jfm.2026.12185 Published online by Cambridge University Press

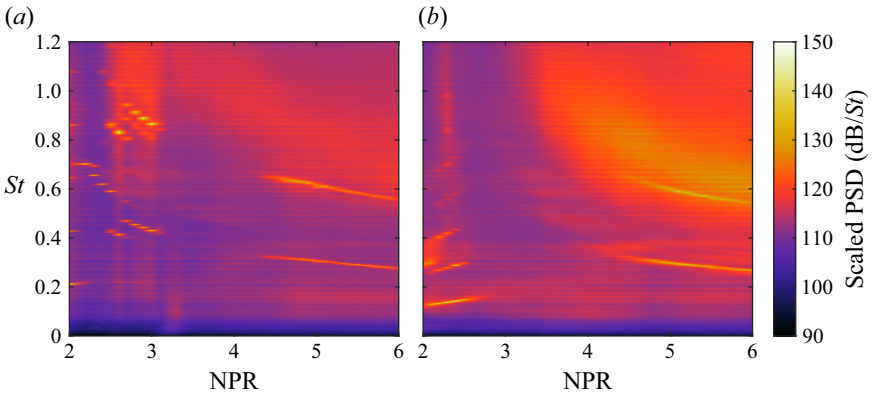


Figure 23. Scaled PSD spectrograms for nozzles (*a*) TA2L8 and (*b*) TA2L15.

long as the interaction between the KH wavepacket and the shock-cell structure can transfer energy to the wavenumber range that the GJM can be supported by the flow equation (1.2). For nozzle TA2L15, the shock-cell wavenumber decreases monotonically with increasing NPR and (1.2) is always satisfied. As a result, screech was observed in a continuous NPR range (figure 19*e*,*f*). In the case of nozzle TA2L8, at low NPRs, the triadic interaction condition can be satisfied, leading to the existence of $m = 1$ screech. However, as the flow develops, the shock-cell wavenumber increases, violating the resonance condition for this azimuthal mode. But under this condition, (1.2) is satisfied for the $m = 0$ mode. Consequently, the $m = 1$ screech branch truncates, and the $m = 0$ branch emerges. By further increasing NPR, the wavenumber of the shock cells monotonically decreases until (1.2) is satisfied again for the $m = 1$ mode, and this screech branch reappears.

As demonstrated, the changes in the shock-cell structure can significantly influence the screech behaviour of a nozzle, and the existence of this resonance can be explained using the triadic interaction framework. Our attention now shifts towards indicating the nozzle characteristics that drive these changes. As elucidated earlier, the examined nozzles share the same area ratio, but their screech characteristics are notably different. Extending the analysis to nozzle TA2L6, it can be seen that the screech behaviour of this nozzle (figure 19*a*,*b*) is similar to that of nozzle TA2L15 (figure 19*e*,*f*) with continuous screech branches existing in a wide NPR range. The difference in screech behaviours suggests that the nozzle area ratio is not the parameter that defines resonance characteristics for this problem. Instead, one can notice that there are similarities between nozzles TA2L8, TA4L8 and TA6L8 in their resonance patterns. All of them exhibit screech branches that exist in a narrow NPR range and then terminate or switch to another branch; and from schlieren images , changes in shock-cell structure in these nozzles were observed at the termination points of the screech branches. An interesting observation is that these nozzles share the same divergence angle (18.5°) but have different area ratios. This observation suggests that the divergence angle plays an important role in dictating the screech behaviour in rocket nozzles. However, given that the current dataset is limited in geometric parameters and the range of operating conditions, this argument will require further validation in future work.

Finally, after confirming that screech does exist in the FSS regime, the acoustic signature of this resonance loop in this flow pattern will be briefly examined. Details of the acoustic measurements and data processing can be found in Appendix E. Shown in figure 23 are the scaled PSD spectrograms for nozzles TA2L8 and TA2L15. It can be seen that the acoustic spectrograms for both nozzles share some similar features with the SPOD spectrograms

https://doi.org/10.1017/jfm.2026.12185 Published online by Cambridge University Press

presented in figure 19(*c–f*) with peaks at the screech frequency. However, there are certain operating conditions (i.e. NPRs $\approx [3.3 : 4.2]$ for nozzle TA2L8 and NPRs $\approx [2.8 : 4]$ for nozzle TA2L15) where the acoustic signature of screech is not as prominent as in the SPOD spectra. The absence of tonal sound was also reported in Jaunet *et al.* (2017).

Several possibilities can lead to this observation. Firstly, the directivity of the screech acoustic radiation or the region of acoustic emission might not align with the microphone location, resulting in a weak acoustic signature in some operating conditions. Secondly, it could be the nature of the FSS pattern itself, such as the double shear layers that trap the acoustic wave, preventing it from radiating to the far field. And for the case of Jaunet *et al.* (2017), since the nozzle used in that study is longer than those used in this work, with flow features remaining inside the nozzle, the acoustic wave might be blocked by the nozzle wall and not radiate to the far field. With the current techniques, it cannot be determined which of these possibilities is the most likely. Further investigations are needed to clarify this observation.

5. Conclusions

In summary, this work aims to shed light on the proposed hypothesis that screech is responsible for the high-amplitude discrete-frequency modes observed in the FSS regime. The study was conducted on five different TOP nozzles with various dimensions operated at NPRs $= [2 : 6]$. Via SPOD analysis performed on schlieren images, distinct resonance peaks were observed for all nozzles for both $m = 0$ and $m = 1$ azimuthal modes. The mode shapes and wavenumber spectra reveal the presence of upstream- and downstream-travelling waves. The downstream-travelling wave was identified as the KH instability wave, which was found to be confined in the shear-layer regions of the supersonic annulus. The upstream-travelling wave was recognised as the GJM, which possesses a subsonic phase velocity and gains more radial support than the KH waves.

Linear stability analysis was performed on the mean flow obtained from RANS simulations to characterise the waves supported by the flow. The analysis reconfirms the existence of the KH waves and the GJM as observed experimentally. For the KH waves, two discrete unstable modes were found corresponding to the inner and outer shear layers of the supersonic annulus. Both of them are supported by the flow for a wide range of frequencies. The outer KH wave possesses a higher growth rate and radial support than the inner KH wave for all frequencies in the studied range for both azimuthal modes. Shifting to the GJM, this wave manifests on the spectra as a neutrally stable wave with a subsonic phase velocity, which agrees well with the SPOD results and its theoretical description in the literature (Nogueira *et al.* 2024). Unlike the KH waves, the GJM only exists in a narrow frequency range for both azimuthal modes. It was discovered that at the frequency ranges where resonance was observed, the GJM of the $m = 0$ azimuthal mode manifests a second-order radial structure with two peaks and the primary peak is located at the jet core. In contrast, the $m = 1$ GJM exhibits a first-order radial structure with a single peak located between the shear layers.

STIM, based on the triadic interaction framework, was employed and successfully predicted the resonant frequencies for all cases. This model was purely developed and well validated to predict screech frequencies. The fact that a model for jet screech is able to correctly predict all frequencies and mode shapes across the range of data presented herein is a robust confirmation of the hypothesis of Jaunet *et al.* (2017): the discrete frequencies observed in the FSS regime are indeed the consequence of the jet-screech phenomenon. However, the physical mechanism underpinning the self-sustained screech loop identified in the present study differs from that proposed by Martelli *et al.* (2020). The SPOD spatial

https://doi.org/10.1017/jfm.2026.12185 Published online by Cambridge University Press

modes reveal that the resonance exhibits features of a classical screeching jet, where the triadic interaction region is located further downstream, rather than being confined between the Mach disk and the downstream normal shock. Additionally, it is the KH waves arising from the shear-layer instability that serve as the downstream disturbances rather than vortices shed from the distortion of the Mach disk. These findings are consistent with Bakulu *et al.* (2021). Given that the operating conditions and the nozzle geometries used in the present study are different from those in Martelli *et al.* (2020), it is possible that screech loops can be sustained by different mechanisms under different conditions.

Further investigations reveal that screech behaviour varies significantly between nozzle geometries. For some nozzles, screech exists in a wide and continuous NPR range for both azimuthal modes, while for some nozzles, screech only exists in a narrow NPR range and terminates or shifts to different branches. For the latter cases, it was discovered that the changes in screech behaviours are associated with the abrupt changes in the shock structure and wavenumber. These arguments were supported by the successful predictions of the resonant frequencies using STIM for all nozzles. Examining the nozzle characteristics suggests that the nozzle divergence angle plays an important role in altering the shock structure and, consequently, the screech behaviour.

There remain open questions that need to be addressed. Firstly, even though the existence of a screech resonance loop is confirmed in the FSS regime, this work has not yet proposed a complete feedback loop mechanism. Specifically, it is unclear if the inner or outer or both KH waves play a role in sustaining the screech loop due to the limitations of LSA, such as the linear nature and the locally parallel assumption. The current experiment set-up does not provide visualisation around the separation point, preventing the identification of the receptivity region. Global stability analysis can be performed in future work to provide more insights into this problem.

Secondly, despite confirming the existence of screech in the FSS regime, the relation between the screech loop and side-load generation was not studied. It is still unclear what component of the screech loop can drive the unsteady oscillation of the shock structure and how it does that. The role of the nozzle divergence angle in influencing the flow structure has been observed. However, the underlying mechanism that drives the flow structure change is still unknown. To address these questions, the use of high-fidelity numerical simulations such as large-eddy simulations is needed to gain a better understanding of the flow dynamics and the screech-side load contribution.

Lastly, it was observed that, in certain operating conditions, distinct tonal sounds were not recorded in the acoustic measurements even though the screech loop was active. It remains unclear whether this is due to the directivity of the acoustic radiation, the region of acoustic emission, the nature of the FSS pattern or, in the case of Jaunet *et al.* (2017), the nozzle wall blocking the acoustic wave. Further investigations are needed to clarify this observation. This could be achieved by using multiple microphones to perform acoustic measurements at different axial and azimuthal locations and using nozzles with different lengths to examine the effect of the nozzle wall on the acoustic radiation.

Supplementary material. Computational Notebook files are available as supplementary material at https://doi.org/10.1017/jfm.2026.12185 and online at https://www.cambridge.org/S0022112026121855/JFM-Notebooks.

Acknowledgements. The authors acknowledge Alexander Linossier for providing the Deker Bayesian optimisation code used in the RANS turbulence model tuning.

Funding. The authors acknowledge the support from the Australian Research Council under the Future Fellowship scheme: FT220100679 and Discovery Early Career Researcher Award scheme: DE240100933.

Declaration of interests. The authors report no conflict of interest.

https://doi.org/10.1017/jfm.2026.12185 Published online by Cambridge University Press

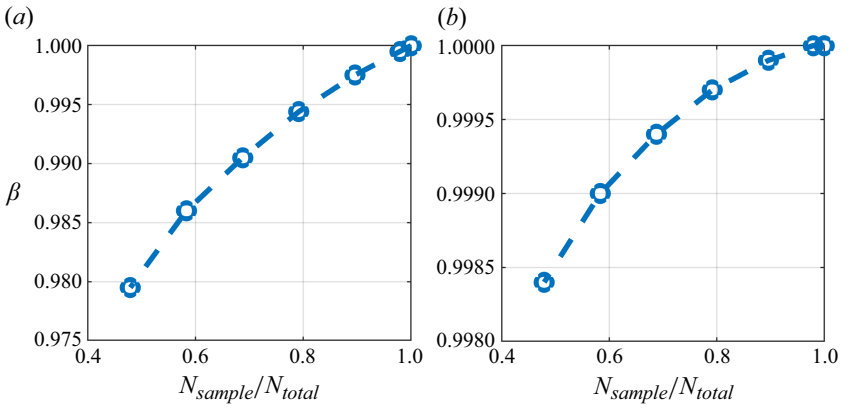


Figure 24. Convergence of the SPOD mode shapes (ϕ) associated with the resonance peaks for nozzle TA6L8 at NPR = 4: (*a*) $m = 0$ mode and (*b*) $m = 1$ mode.

Appendix A. The SPOD sensitivity analysis

A SPOD convergence study for the resonance mode shapes and energies was conducted using jackknife resampling of fast Fourier transform blocks and performing SPOD on the resampled data. For the spatial mode shapes, the convergence was quantified by computing the normalised inner product between the resampled SPOD mode shape and the SPOD mode shape computed by the full set of data. The inner product is defined as

$$\beta_i = \frac{\langle \phi_i, \bar{\phi} \rangle}{\|\phi_i\| \|\bar{\phi}\|}. \tag{A1}$$

Here, ϕ_i is the resampled SPOD mode shape and $\bar{\phi}$ is the SPOD mode shape computed by the full set of data. Parameter β_i indicates the correlation between the two mode shapes, with a value of 1 indicating perfect correlation and a value of 0 indicating orthogonality. The blocks were selected in a continuous manner with one block shifted for each permutation. The results were then averaged over all permutations to obtain the average value of β. The number of permutations for each case varies such that all the fast Fourier transform blocks are used. The outcomes of this analysis are shown in figure 24. It can be seen that the mode shapes associated with the resonance structure converge for both azimuthal modes with a minimum β value of ≈ 0.98 even with ≈ 60 % of the blocks removed.

Similarly, the convergence of the SPOD mode energy was quantified by computing the normalised absolute difference between the resampled SPOD mode energy and the SPOD mode energy computed by the full set of data and the results are shown in figure 25. There is good convergence for both azimuthal modes up to ≈ 30 % of the blocks removed, with a maximum error of ≈ 7 %. With more blocks removed, greater errors are observed, especially for the $m = 1$ mode. This is due to the frequency drift observed in figures 5 and 26, which leads to lower energy content in these snapshots. However, since the whole dataset was used for the SPOD analysis and the resonance mode shapes are well converged, the discussed error in the mode energy does not affect this study.

Attention is turned to the frequency drift of the resonance peaks observed in figure 5. Shown in figure 26 is the time–frequency analysis of the first SPOD mode energy for the studied case. The two peaks manifest in this figure as the two bright horizontal bands. It can be seen that the $St = 0.293$ peak is only active in the early stage of the sampling

https://doi.org/10.1017/jfm.2026.12185 Published online by Cambridge University Press

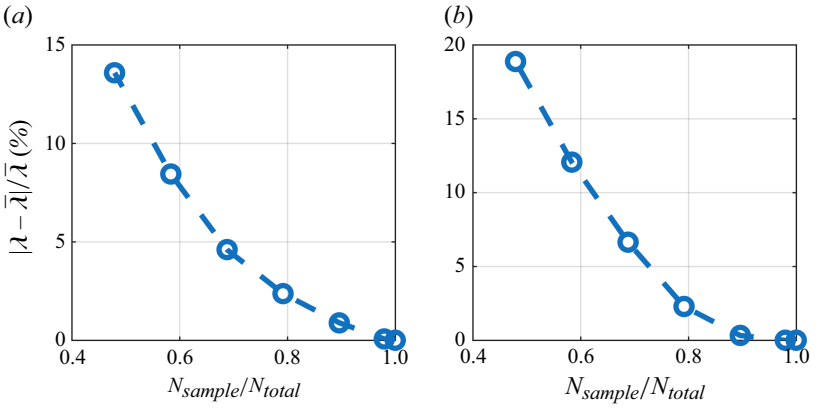


Figure 25. Convergence of the SPOD mode energy (λ) associated with the resonance peaks for nozzle TA6L8 at NPR = 4: (*a*) $m = 0$ mode and (*b*) $m = 1$ mode.

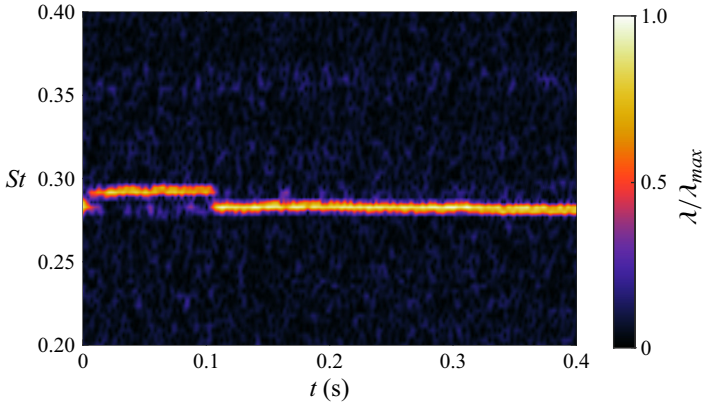


Figure 26. Time–frequency analysis of the first SPOD mode energy for nozzle TA6L8 at NPR = 4.

period, which can be attributed to the initial intermittent behaviour of the flow. When the flow reaches steady state, only the $St = 0.283$ peak remains. Considering that the SPOD mode shapes and energies for this peak are well converged for the current dataset, it can be assumed that the frequency drift does not affect the results of this study.

Appendix B. Sensitivity analysis of isolated-SPOD-mode-shape window width

In this appendix, the sensitivity of the isolated SPOD mode shapes (discussed in figure 8) to the window size is analysed. Shown in table 5 is the window size used in this study. The analysis was conducted by computing the normalised inner product (similar to (A1)) between the isolated SPOD mode shape with different window sizes and the isolated SPOD mode shape using the window size specified in table 5. For each iteration, the window size was increased by $\Delta k_x D_j = 1$ and three iterations were performed for each peak.

The results of the analysis are demonstrated in figure 27. In general, the isolated SPOD mode shapes are well converged for all peaks. For the $m = 0$ mode, the upstream peak

https://doi.org/10.1017/jfm.2026.12185 Published online by Cambridge University Press

	$k_{u,min}$	$k_{u,max}$	$k_{d,min}$	$k_{d,max}$
$m=0$ peak	−4.5	−1.6	1.9	3.6
$m=1$ peak	−4	−2	2.4	3.9

Table 5. Isolated SPOD wavenumber window for the resonance peaks for nozzle TA6L8 at NPR = 4. Here, $k_{u,min}$ and $k_{u,max}$ are the minimum and maximum wavenumbers of the upstream window, while $k_{d,min}$ and $k_{d,max}$ are the minimum and maximum wavenumbers of the downstream window.

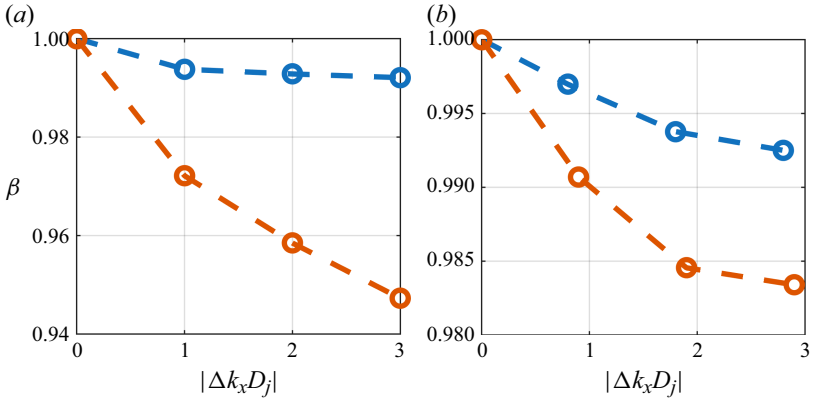


Figure 27. Convergence of the isolated SPOD mode shapes associated with the resonance peaks for nozzle TA6L8 at NPR = 4 with different window widths: (*a*) $m=0$ mode and (*b*) $m=1$ mode. Orange curve: upstream peak; blue curve: downstream peak.

Nozzle	NPR	k_{sh1} (RANS)	k_{sh2} (RANS)	k_{sh1} (Exp)	k_{sh2} (Exp)	k_{sh1} Error (%)	k_{sh2} Error (%)
TA2L8	4	7.14	9.12	6.73	8.43	6.09	8.19
TA2L15	4	5.35	6.94	5.13	6.44	4.29	7.76

Table 6. Comparison of k_{sh} obtained from RANS with default turbulence parameters and experimental data.

(orange curve) is more sensitive to the window size than the downstream one. However, even with the greatest window size, the correlation value is still ≈ 0.95. Better convergence is observed for the $m=1$ peaks with a minimum correlation value of ≈ 0.984. Hence, the isolated SPOD mode shapes are not significantly affected by the window size, and the current window size used in this study is sufficient to capture the mode shapes of travelling waves.

Appendix C. Tuned turbulence parameters for RANS simulations

Figure 28 and table 6 show the reference errors of the RANS calculation using default turbulence parameter values. It can be seen that the shock-cell structures are not accurately captured in either case, and the errors differ between the two. For that reason, it is necessary to conduct the tuning campaign for each RANS case independently. The tuning

https://doi.org/10.1017/jfm.2026.12185 Published online by Cambridge University Press

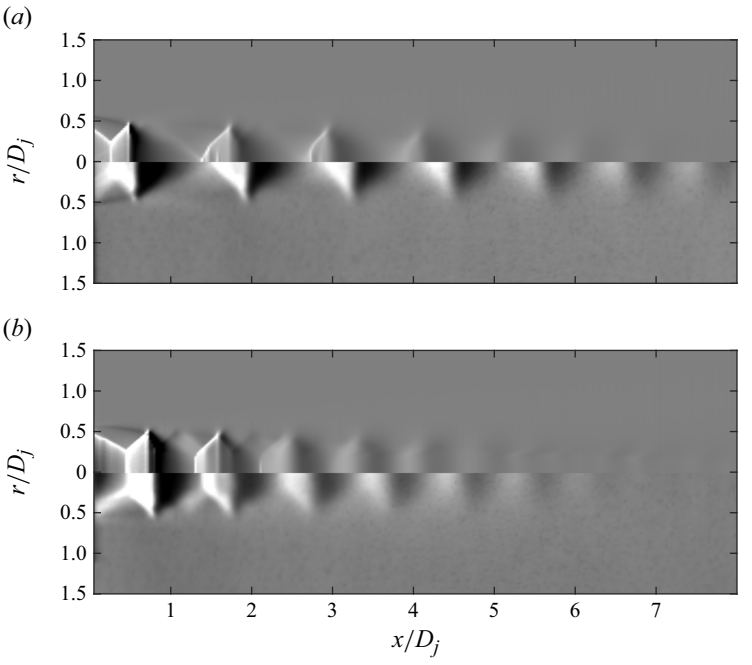


Figure 28. Shock structure comparison between RANS simulation with default turbulence parameters (top half of each panel) and mean schlieren image (bottom half of each panel) at NPR = 4 for (*a*) nozzle TA2L15 and (*b*) nozzle TA2L8. The RANS streamwise density gradient was reconstructed into a three-dimensional field with axisymmetric assumption and path-integrated to facilitate the comparison.

approach started with the default set of parameters for the $k-\omega$ SST model, which can be found in Menter *et al.* (2003). The turbulence model equations were specified in Menter & Esch (2001). Since this model contains several empirical coefficients, a sensitivity analysis was conducted to identify the most influential parameters affecting the shock-cell structure. It was found that σ_{k2}, $\sigma_{\omega 2}$, β_2 and α_2 are the most significant parameters. They lie in the source and sink terms of the model equations that govern the production and dissipation of k and ω, and hence control the shear-layer spreading and potential-core decay rate of the mean flow. Since these parameters are only effective in the free-stream turbulence, they can be tuned without significantly impacting the near-wall features of the wall, such as the separation point and the boundary-layer characteristics. Hence, a systematic tuning of these parameters accelerated by the utilisation of Bayesian optimisation was then carried out for each nozzle and operating condition to achieve the best agreement with the mean schlieren images. Given that the relation between the parameters and the shock-cell wavelength is monotonic, the optimised range for each parameter was determined by the values of that parameter where RANS calculation significantly over- and underpredicts k_{sh} while keeping other parameters at their default values. The final set of tuned parameters for all the cases is summarised in table 7. A comparison of k_{sh} between RANS simulation and experiments for all cases can be found in table 8. There are cases where the values of k_{sh_2} are not used for the tuning process. This is because the shock wavenumber spectrum manifests as a broad peak, so the values of k_{sh_2} cannot be identified. In these cases, only k_{sh_1} was used for the tuning process. It can be observed from table 7 that $\sigma_{\omega 2}$ and β_2 were kept constant for all cases. This is because, to minimise the computational cost, the tuning process was first performed on fewer parameters, and if unsatisfactory results were

https://doi.org/10.1017/jfm.2026.12185 Published online by Cambridge University Press

Nozzle	NPR	σ_{k2}	$\sigma_{\omega 2}$	β_2	α_2
TA2L6	3	0.5	0.856	0.0828	0.55
	3.5	1.0	0.856	0.0828	0.55
	4	0.51	0.856	0.0828	0.57
	4.5	1.0	0.856	0.0828	0.65
	5	1.0	0.856	0.0828	0.60
TA2L8	3	0.1	0.856	0.0828	0.53
	3.5	1.0	0.856	0.0828	0.45
	4	1.0	0.856	0.0828	0.55
	4.5	1.0	0.856	0.0828	0.55
	5	0.5	0.856	0.0828	0.55
TA2L15	3	0.5	0.856	0.0828	0.55
	3.5	1.0	0.856	0.0828	0.45
	4	0.5	0.856	0.0828	0.55
	4.5	1.0	0.856	0.0828	0.45
	5	0.7	0.856	0.0828	0.55
TA4L8	3	0.1	0.856	0.0828	0.51
	3.5	1.0	0.856	0.0828	0.67
	4	0.5	0.856	0.0828	0.55
	4.5	1.0	0.856	0.0828	0.615
	5	1.0	0.856	0.0828	0.64
TA6L8	3	1.0	0.856	0.0828	0.49
	3.5	0.1	0.856	0.0828	0.55
	4	1.0	0.856	0.0828	0.67
	4.5	0.5	0.856	0.0828	0.55
	5	0.5	0.856	0.0828	0.55

Table 7. The RANS tuned parameters.

obtained, the process would be repeated with more parameters. It was found that tuning σ_{k2} and α_2 alone was sufficient to achieve good agreement with the experimental results for this study. However, $\sigma_{\omega 2}$ and β_2 values are shown for completeness and to provide a reference for future studies.

https://doi.org/10.1017/jfm.2026.12185 Published online by Cambridge University Press

Nozzle	NPR	k_{sh1} (RANS)	k_{sh2} (RANS)	k_{sh1} (Exp)	k_{sh2} (Exp)	k_{sh1} Error (%)	k_{sh2} Error (%)
TA2L6	3	5.82	7.14	5.73	7.41	1.57	3.64
	3.5	5.21	6.56	5.21	6.96	0.00	5.75
	4	4.76	5.95	4.80	6.08	0.83	2.14
	4.5	4.68	5.49	4.63	5.73	1.08	4.19
	5	4.79	5.83	4.66	5.81	2.79	0.34
TA2L8	3	6.38	7.70	6.33	8.30	0.79	7.23
	3.5	6.95	8.88	7.21	8.92	3.61	0.45
	4	6.74	8.33	6.73	8.43	0.15	1.19
	4.5	6.31	7.73	6.13	7.58	2.94	1.98
	5	5.21	6.67	5.49	6.75	5.10	1.19
TA2L15	3	7.51	9.20	7.58	9.60	0.92	4.17
	3.5	5.60	7.33	5.91	7.53	5.25	2.66
	4	5.15	6.54	5.13	6.44	0.39	1.55
	4.5	4.27	5.69	4.57	5.67	6.56	0.35
	5	3.96	5.00	4.16	5.20	4.81	3.85
TA4L8	3	6.01	7.70	5.97	8.22	0.67	6.33
	3.5	5.21	NaN	5.15	NaN	1.17	NaN
	4	7.14	8.92	7.04	8.83	1.42	1.02
	4.5	7.12	8.34	7.17	8.50	0.70	1.88
	5	6.88	7.92	6.79	8.03	1.33	1.37
TA6L8	3	6.57	NaN	6.57	NaN	0.00	NaN
	3.5	5.60	6.95	5.51	7.64	1.63	9.03
	4	5.16	6.15	5.13	6.64	0.58	7.38
	4.5	7.12	8.95	7.03	8.53	1.28	4.92
	5	7.50	10.21	7.29	10.60	2.88	3.65

Table 8. Comparison of k_{sh} obtained from RANS and experimental data.

Appendix D. The LSA operator

In this appendix, the LSA operators used in this work are presented. The linearised inviscid Navier–Stokes equation (shown in (2.4)) can be written in matrix form as

$$\boldsymbol{L} = \begin{bmatrix} \boldsymbol{L_{11}} & \boldsymbol{0} & \boldsymbol{L_{13}} & \boldsymbol{L_{14}} & \boldsymbol{0} \\ \boldsymbol{0} & \boldsymbol{L_{22}} & \boldsymbol{L_{23}} & \boldsymbol{0} & \boldsymbol{0} \\ \boldsymbol{L_{31}} & \boldsymbol{0} & \boldsymbol{L_{33}} & \boldsymbol{0} & \boldsymbol{L_{35}} \\ \boldsymbol{0} & \boldsymbol{0} & \boldsymbol{0} & \boldsymbol{L_{44}} & \boldsymbol{L_{45}} \\ \boldsymbol{0} & \boldsymbol{0} & \boldsymbol{L_{53}} & \boldsymbol{L_{54}} & \boldsymbol{L_{55}} \end{bmatrix}, \tag{D1}$$

with

$$\boldsymbol{L_{11}} = -\mathrm{i}\omega, \tag{D2}$$

$$\boldsymbol{L_{13}} = \frac{\partial \bar{\nu}}{\partial r} - \bar{\nu}\frac{\partial}{\partial r} - \frac{\bar{\nu}}{r}, \tag{D3}$$

$$\boldsymbol{L_{14}} = -\frac{\mathrm{i}m}{r}\bar{\nu}, \tag{D4}$$

https://doi.org/10.1017/jfm.2026.12185 Published online by Cambridge University Press

$$\boldsymbol{L_{22}} = -\mathrm{i}\omega, \tag{D5}$$

$$\boldsymbol{L_{23}} = \frac{\partial \bar{u_x}}{\partial r}, \tag{D6}$$

$$\boldsymbol{L_{31}} = \frac{\partial \bar{p}}{\partial r}, \tag{D7}$$

$$\boldsymbol{L_{33}} = -\mathrm{i}\omega, \tag{D8}$$

$$\boldsymbol{L_{35}} = \bar{\nu}\frac{\partial}{\partial r}, \tag{D9}$$

$$\boldsymbol{L_{44}} = -\mathrm{i}\omega, \tag{D10}$$

$$\boldsymbol{L_{45}} = \frac{\mathrm{i}\bar{\nu}m}{r}, \tag{D11}$$

$$\boldsymbol{L_{53}} = \frac{\gamma\bar{p}}{r} + \frac{\partial \bar{p}}{\partial r} + \gamma\bar{p}\frac{\partial}{\partial r}, \tag{D12}$$

$$\boldsymbol{L_{54}} = \frac{\mathrm{i}m\gamma\bar{p}}{r}, \tag{D13}$$

$$\boldsymbol{L_{55}} = -\mathrm{i}\omega. \tag{D14}$$

And matrix $\boldsymbol{R}$ is

$$\boldsymbol{R} = \begin{bmatrix} \boldsymbol{R_{11}} & \boldsymbol{R_{12}} & \boldsymbol{0} & \boldsymbol{0} & \boldsymbol{0} \\ \boldsymbol{0} & \boldsymbol{R_{22}} & \boldsymbol{0} & \boldsymbol{0} & \boldsymbol{R_{25}} \\ \boldsymbol{0} & \boldsymbol{0} & \boldsymbol{R_{33}} & \boldsymbol{0} & \boldsymbol{0} \\ \boldsymbol{0} & \boldsymbol{0} & \boldsymbol{0} & \boldsymbol{R_{44}} & \boldsymbol{0} \\ \boldsymbol{0} & \boldsymbol{R_{52}} & \boldsymbol{0} & \boldsymbol{0} & \boldsymbol{R_{55}} \end{bmatrix}, \tag{D15}$$

with

$$\boldsymbol{R_{11}} = -\mathrm{i}\bar{u_x}, \tag{D16}$$

$$\boldsymbol{R_{12}} = \mathrm{i}\bar{\nu}, \tag{D17}$$

$$\boldsymbol{R_{22}} = -\mathrm{i}\bar{u_x}, \tag{D18}$$

$$\boldsymbol{R_{25}} = -\mathrm{i}\bar{\nu}, \tag{D19}$$

$$\boldsymbol{R_{33}} = -\mathrm{i}\bar{u_x}, \tag{D20}$$

$$\boldsymbol{R_{44}} = -\mathrm{i}\bar{u_x}, \tag{D21}$$

$$\boldsymbol{R_{52}} = -\mathrm{i}\gamma\bar{p}, \tag{D22}$$

$$\boldsymbol{R_{55}} = -\mathrm{i}\bar{u_x}. \tag{D23}$$

https://doi.org/10.1017/jfm.2026.12185 Published online by Cambridge University Press

Appendix E. Acoustic measurement procedure

The acoustic data were acquired using a GRAS type 46BE 1/4 inch pre-amplified free-field microphone located at $x/D_t \approx 8.5$ from the TA2L8 nozzle exit and $r/D_t \approx 39.5$ from the jet centreline. The nominal frequency band of this microphone is 4 Hz to 80 kHz. For each case, acoustic data were recorded at a sampling frequency of $f_s = 200$ kHz for a duration of 5 s, ensuring the Nyquist frequency is sufficiently high to capture the screech tones.

The frequency spectra were computed using the acoustic data following the procedure shown in Beekman *et al.* (2024). Here, the pressure signal from the microphone was transformed using the Welch method (Welch 1967) with a Hann window of $N_{fft} = 4096$ samples and 50 % overlap between adjacent segments. The auto-spectrum strength ($\mathrm{Pa}^2\ \mathrm{Hz}^{-1}$) was then computed as follows:

$$\hat{P}(f) = E[\hat{p}(f)\hat{p}^*(f)]. \tag{E1}$$

Here, the asterisk denotes the complex conjugate and $E[\cdot]$ represents the averaged value over all segments. Then the scaled PSD for each St value was calculated as (Brès *et al.* 2018)

$$\text{Scaled PSD}(St) = 10\log_{10}\left[\frac{\hat{P}(f)}{p_{ref}^2}\frac{U_j}{D_j}\frac{\rho_\infty^2}{\rho_j^2}\frac{1}{M_a^4}\right]. \tag{E2}$$

In this formulation, $p_{ref} = 2 \times 10^{-5}$ Pa is the reference pressure, ρ_j is the ideally expanded jet exit density and M_a is the acoustic Mach number, which can be calculated as

$$M_a = \frac{U_j}{c_\infty}. \tag{E3}$$

References

Baars, W.J. & Tinney, C.E. 2013 Transient wall pressures in an overexpanded and large area ratio nozzle. *Exp. Fluids* **54** (2), 1468.

Baars, W.J., Tinney, C.E., Ruf, J.H., Brown, A.M. & McDaniels, D.M. 2012 Wall pressure unsteadiness and side loads in overexpanded rocket nozzles. *AIAA J.* **50** (1), 61–73.

Bakulu, F., Lehnasch, G., Jaunet, V., Goncalves da Silva, E. & Girard, S. 2021 Jet resonance in truncated ideally contoured nozzles. *J. Fluid Mech.* **919**, A32.

Beekman, J., Weightman, J., Jordan, P., Nogueira, P.A.S. & Edgington-Mitchell, D.M. 2024 Acoustic characterisation of subsonic and supersonic elliptical jets. In *30th AIAA/CEAS Aeroacoustics Conference (2024)*. American Institute of Aeronautics and Astronautics.

Brès, G.A., Jordan, P., Jaunet, V., Le Rallic, M., Cavalieri, A.V.G., Towne, A., Lele, S.K., Colonius, T. & Schmidt, O.T. 2018 Importance of the nozzle-exit boundary-layer state in subsonic turbulent jets. *J. Fluid Mech.* **851**, 83–124.

Briggs, R.J. 1964 *Electron-Stream Interaction With Plasmas*. MIT Press.

Cavalieri, A.V.G., Rodríguez, D., Jordan, P., Colonius, T. & Gervais, Y. 2013 Wavepackets in the velocity field of turbulent jets. *J. Fluid Mech.* **730**, 559–592.

Dumnov, G. 1996 Unsteady side-loads acting on the nozzle with developed separation zone. arXiv: https://arc.aiaa.org/doi/pdf/10.2514/6.1996-3220.

Edgington-Mitchell, D. 2019 Aeroacoustic resonance and self-excitation in screeching and impinging supersonic jets – a review. *Intl J. Aeroacoust.* **18** (2–3), 118–188.

Edgington-Mitchell, D., Jaunet, V., Jordan, P., Towne, A., Soria, J. & Honnery, D. 2018 Upstream-travelling acoustic jet modes as a closure mechanism for screech. *J. Fluid Mech.* **855**, R1.

Edgington-Mitchell, D., Li, X., Liu, N., He, F., Wong, T.Y., Mackenzie, J. & Nogueira, P. 2022 A unifying theory of jet screech. *J. Fluid Mech.* **945**, A8.

Edgington-Mitchell, D., Wang, T., Nogueira, P., Schmidt, O., Jaunet, V., Duke, D., Jordan, P. & Towne, A. 2021 Waves in screeching jets. *J. Fluid Mech.* **913**, A7.

Frey, M. & Hagemann, G. 1999 Flow separation and side-loads in rocket nozzles. In *35th Joint Propulsion Conference and Exhibit*. American Institute of Aeronautics and Astronautics.

https://doi.org/10.1017/jfm.2026.12185 Published online by Cambridge University Press

GLOOR, M., OBRIST, D. & KLEISER, L. 2013 Linear stability and acoustic characteristics of compressible, viscous, subsonic coaxial jet flow. *Phys. Fluids* **25** (8), 084102.
GOJON, R., BOGEY, C. & MIHAESCU, M. 2018 Oscillation modes in screeching jets. *AIAA J.* **56** (7), 2918–2924.
GREENSHIELDS, C. 2023 *OpenFOAM v11 User Guide*. The OpenFOAM Foundation.
IVELJA, R., EDGINGTON-MITCHELL, D., MAIGLER, M. & NOGUEIRA, P.A.S. 2024 Modal analysis of screeching elliptical jets. *J. Fluid Mech.* **1000**, A68.
JAUNET, V., ARBOS, S., LEHNASCH, G. & GIRARD, S. 2017 Wall pressure and external velocity field relation in overexpanded supersonic jets. *AIAA J.* **55** (12), 4245–4257.
JAUNET, V. & LEHNASCH, G. 2025 Linear dynamics of over-expanded annular supersonic jets. *J. Fluid Mech.* **1009**, A32.
JORDAN, P., JAUNET, V., TOWNE, A., CAVALIERI, A.V.G., COLONIUS, T., SCHMIDT, O. & AGARWAL, A. 2018 Jet–flap interaction tones. *J. Fluid Mech.* **853**, 333–358.
LESSHAFFT, L. & HUERRE, P. 2007 Linear impulse response in hot round jets. *Phys. Fluids* **19** (2), 024102.
LINOSSIER, A. 2025 Deker - process optimisation. Available at: https://www.dekerai.com.
LUMLEY, J.L. 1970 *Stochastic Tools in Turbulence*. Academic Press.
MARTELLI, E., SACCOCCIO, L., CIOTTOLI, P.P., TINNEY, C.E., BAARS, W.J. & BERNARDINI, M. 2020 Flow dynamics and wall-pressure signatures in a high-Reynolds-number overexpanded nozzle with free shock separation. *J. Fluid Mech.* **895**, A29.
MENTER, F. & ESCH, T. 2001 Elements of industrial heat transfer prediction. In *16th Brazilian Congress of Mechanical Engineering (COBEM), Nov. 2001*.
MENTER, F.R., KUNTZ, M. & LANGTRY, R. 2003 Ten years of industrial experience with the SST turbulence model. *Heat Mass Transfer* **4** (1), 625–632.
MICHALKE, A. 1965 On spatially growing disturbances in an inviscid shear layer. *J. Fluid Mech.* **23** (3), 521–544.
NAVE, L. & COFFEY, G. 1973 Sea level side loads in high-area-ratio rocket engines. In *9th Propulsion Conference*. American Institute of Aeronautics and Astronautics.
NEKKANTI, A. & SCHMIDT, O.T. 2021 Frequency–time analysis, low-rank reconstruction and denoising of turbulent flows using SPOD. *J. Fluid Mech.* **926**, A26.
NOGUEIRA, P.A.S., CAVALIERI, A.V.G., MARTINI, E., TOWNE, A., JORDAN, P. & EDGINGTON-MITCHELL, D. 2024 Guided-jet waves. *J. Fluid Mech.* **999**, A47.
NOGUEIRA, P.A.S. & EDGINGTON-MITCHELL, D.M. 2021 Investigation of supersonic twin-jet coupling using spatial linear stability analysis. *J. Fluid Mech.* **918**, A38.
NOGUEIRA, P.A.S., JAUNET, V., MANCINELLI, M., JORDAN, P. & EDGINGTON-MITCHELL, D. 2022*a* Closure mechanism of the A1 and A2 modes in jet screech. *J. Fluid Mech.* **936**, A10.
NOGUEIRA, P.A.S., JORDAN, P., JAUNET, V., CAVALIERI, A.V.G., TOWNE, A. & EDGINGTON-MITCHELL, D. 2022*b* Absolute instability in shock-containing jets. *J. Fluid Mech.* **930**, A10.
NOGUEIRA, P.A.S., SELF, H.W.A., TOWNE, A. & EDGINGTON-MITCHELL, D. 2022*c* Wave-packet modulation in shock-containing jets. *Phys. Rev. Fluids* **7** (7), 074608.
NOGUEIRA, P.A.S., WEIGHTMAN, J. & EDGINGTON-MITCHELL, D. 2025 Screech in military-style rectangular nozzles. *AIAA J.* **63** (10), 4210–4222.
PANDA, J. 1999 An experimental investigation of screech noise generation. *J. Fluid Mech.* **378**, 71–96.
PERRAULT-JONCAS, D. & MASLOWE, S.A. 2008 Linear stability of a compressible coaxial jet with continuous velocity and temperature profiles. *Phys. Fluids* **20** (7), 074102.
POWELL, A. 1953 On the mechanism of choked jet noise. *Proc. Phys. Soc. B* **66** (12), 1039–1056.
RAMAN, G. 1999 Supersonic jet screech: half-century from Powell to the present. *J. Sound Vib.* **225** (3), 543–571.
RAO, G.V.R. 1958 Exhaust nozzle contour for optimum thrust. *J. Jet Propul.* **28** (6), 377–382.
SCHMUCKER, R.H. 1984 Flow processes in overexpanded chemical rocket nozzles. Part 2: side loads due to asymmetric separation. *Tech. Rep.* NASA-TM-77395. NTRS Author Affiliations: NASA Headquarters NTRS Document ID: 19840011403 NTRS Research Center: Legacy CDMS (CDMS).
SHAHRIARI, B., SWERSKY, K., WANG, Z., ADAMS, R.P. & DE FREITAS, N. 2016 Taking the human out of the loop: a review of Bayesian optimization. *Proc. IEEE* **104** (1), 148–175.
STARK, R. & HAGEMANN, G. 2007 Current status of numerical flow prediction for separated nozzle flows. In *2nd European Conference for Aero-Space Sciences (EUCASS 2007)*.
TAM, C.K.W., SEINER, J.M. & YU, J.C. 1986 Proposed relationship between broadband shock associated noise and screech tones. *J. Sound Vib.* **110** (2), 309–321.
TAM, C.K.W. & HU, F.Q. 1989 On the three families of instability waves of high-speed jets. *J. Fluid Mech.* **201**, 447–483.

https://doi.org/10.1017/jfm.2026.12185 Published online by Cambridge University Press

Towne, A., Cavalieri, A.V.G., Jordan, P., Colonius, T., Schmidt, O., Jaunet, V. & Brès, G.A. 2017 Acoustic resonance in the potential core of subsonic jets. *J. Fluid Mech.* **825**, 1113–1152.

Towne, A., Schmidt, O.T. & Colonius, T. 2018 Spectral proper orthogonal decomposition and its relationship to dynamic mode decomposition and resolvent analysis. *J. Fluid Mech.* **847**, 821–867.

Tran, C.C., Nogueira, P.A. & Edgington-Mitchell, D.M. 2024 Shock separation and resonance in rocket nozzles. In *30th AIAA/CEAS Aeroacoustics Conference (2024)*. American Institute of Aeronautics and Astronautics.

Tran, C.C., Nogueira, P.A., Weightman, J. & Edgington-Mitchell, D. 2026 Screech resonance in free shock separation. In *32nd AIAA/CEAS Aeroacoustics Conference (2026)*. American Institute of Aeronautics and Astronautics.

Trefethen, L.N. 2000 *Spectral Methods in MATLAB*. Society for Industrial and Applied Mathematics.

Welch, P. 1967 The use of fast Fourier transform for the estimation of power spectra: a method based on time averaging over short, modified periodograms. *IEEE Trans. Audio and Electroacoust.* **15** (2), 70–73.

Westley, R. & Woolley, J. 1975 The near field sound pressures of a choked jet when oscillating in the spinning mode. In *2nd Aeroacoustics Conference*.

Willert, C.E., Mitchell, D.M. & Soria, J. 2012 An assessment of high-power light-emitting diodes for high frame rate schlieren imaging. *Exp. Fluids* **53** (2), 413–421.

https://doi.org/10.1017/jfm.2026.12185 Published online by Cambridge University Press